The gammaproteobacterium Achromatium forms intracellular amorphous calcium carbonate and not (crystalline) calcite

Karim Benzerara, Romain Bolzoni, Caroline Monteil, Olivier Beyssac, Olivier Forni, Béatrice Alonso, Maria Asta, Christopher T. Lefèvre

The gamaproteobacterium *Achromatium* forms intracellular amorphous calcium carbonate and not (crystalline) calcite

Running title: *Achromatium* forms ACC and not calcite

Benzerara Karim[1*], Bolzoni Romain[2], Monteil Caroline[2], Beyssac Olivier[1], Forni Olivier[3], Alonso Béatrice[2], Asta Maria P.[4], Lefevre Christopher[2]

[1]Sorbonne Université, Muséum National d'Histoire Naturelle, UMR CNRS 7590. Institut de Minéralogie, de Physique des Matériaux et de Cosmochimie (IMPMC), 4 Place Jussieu, 75005 Paris, France.

[2]Aix-Marseille University, CNRS, CEA, UMR7265 Institute of Biosciences and Biotechnologies of Aix-Marseille, CEA Cadarache, F-13108 Saint-Paul-lez-Durance, France

[3]Institut de Recherche en Astrophysique et Planétologie (CNRS, Univ. Toulouse, CNES), Toulouse, France

[4]University Grenoble Alpes, CNRS, IRD, IFSTTAR, ISTerre, 38000, Grenoble, France

* Corresponding author

Tel.: +33(0)144277542

E-mail address: karim.benzerara@sorbonne-universite.fr

Acknowledgements

This project has received funding from the CNRS: "Programme national Ecosphère Continentale et Côtière (EC2CO)" (BACCARAT2 – N°13068), the French National Research Agency (SIGMAG: ANR-18-CE31-0003 and PHOSTORE: ANR-19-CE01-0005-02), and the European Union's Horizon 2020 research and innovation programme under the Marie Skłodowska-Curie grant agreement 747597. We thank Fériel Skouri-Panet and Cynthia Travert for user support on the IMPMC Biology facility, and Imène Esteve, Béatrice Doisneau and Stéphanie Delbrel for user support on the IMPMC SEM facility. We declare no conflict of interest.

Data Availability Statement

The data that support the findings of this study are openly available in zenodo at http://doi.org/10.5281/zenodo.4295976 and in NCBI for DNA sequences.

Abstract

Achromatium is a long known uncultured giant gammaproteobacterium forming intracellular $CaCO_3$ that impact C and S geochemical cycles functioning in some anoxic sediments and at oxic-anoxic boundaries. While intracellular $CaCO_3$ granules have first been described as Ca oxalate then colloidal $CaCO_3$ more than one century ago, they have often been referred to as crystalline solids and more specifically calcite over the last 25 years. Such a crystallographic distinction is important since the respective chemical reactivities of amorphous calcium carbonate (ACC) and calcite, hence their potential physiological role and conditions of formation, are significantly different. Here we analyzed the intracellular $CaCO_3$ granules of *Achromatium* cells from Lake Pavin using a combination of Raman microspectroscopy and scanning electron microscopy. Granules in intact *Achromatium* cells were unequivocally composed of amorphous calcium carbonate (ACC). Moreover, ACC spontaneously transformed into calcite when irradiated at high laser irradiance during Raman analyses. Few ACC granules also transformed spontaneously into calcite in lysed cells upon cell death and/or sample preparation. Overall, the present study supports the original claims that intracellular Ca-carbonates in *Achromatium* are amorphous and not crystalline. In that sense, *Achromatium* is similar to a diverse group of Cyanobacteria and a recently discovered magnetotactic alphaproteobacterium , which all form intracellular ACC. The implications for the physiology and ecology of *Achromatium* are discussed. Whether the mechanisms responsible for the preservation of such unstable compounds in these bacteria are similar to those involved in numerous ACC-forming eukaryotes remains to be discovered. Last, we recommend to future studies addressing the crystallinity of $CaCO_3$ granules in *Achromatium* cells recovered from diverse environments all over the world to take care of the potential pitfalls evidenced by the present study.

Keywords: Raman; intracellular biomineralization; micromanipulation; ACC

1. Introduction

Achromatium oxaliferum has first been fully described by Schewiakoff (1893). Since then, it has been shown that the genus *Achromatium* groups a diversity of giant colorless sulfur-oxidizing bacterial species which form intracellular elemental S^0 and $CaCO_3$ granules (Gray & Head, 2014). They are widely distributed worldwide at the oxic-anoxic boundary in sediments of freshwater, brackish and marine environments (Ionescu et al., 2020; Salman et al., 2015). Since they can represent a relatively high biovolume, up to 90% of the total microbial volume in a sediment, they have received particular attention. No strain has been cultivated so far but culture-independent methods have been used to infer their physiology and ecology (e.g., Ionescu et al., 2017; Mansor et al., 2015). *Achromatium* cells have been reported to live in the sulfate reduction zone, sometimes in areas of low free sulfide activity, at least for freshwater representatives (Gray & Head, 2014). They oxidize sulfide to elemental sulfur using O_2 or possibly nitrates (Salman et al., 2015). Some populations have been reported to be autotroph for C while others might be organotroph (Gray et al., 1999). *Achromatium* cells may have a significant role in local geochemical cycles of Ca since they form large amounts of intracellular $CaCO_3$ granules. Moreover, they sometimes produce these granules in solutions undersaturated with all Ca-carbonate mineral phases. In these sediments, *Achromatium* cells are the sole carriers of Ca-carbonates (Gray & Head, 2014). Consistently, freshwater sediments from a wetland region close to Rydal Water (UK) have been reported to show a correlation between the solid-phase calcium content and *Achromatium* cell numbers (Head et al., 2000). Since the dynamics of the cells is associated with the dynamics of the oxic-anoxic boundary, it creates a unique connection between variations of redox conditions and carbonate formation.

The function of the intracellular $CaCO_3$ granules has been widely questioned. For example, it has been suggested that these intracellular Ca-carbonate granules may buffer intracellular pH variations associated with sulfur oxidation (e.g., Salman et al., 2015). This idea has been

supported by the recent observations that these Ca-carbonate granules dissolved when cells were exposed to oxygen and sulfur oxidation was promoted (Yang et al., 2019). In contrast, Schorn et al. (2020) suggested that the $CaCO_3$ granules are located in the periplasmic space of *Achromatium* cells, therefore raising questions about this intracellular pH buffering function of $CaCO_3$. An alternative, suggested and also debated, function for $CaCO_3$ granules is that they may serve as ballasts in *Achromatium* and anchor cells to the sediment close to the oxic-anoxic boundary (N. Gray & Head, 2014).

All members of the *Achromatium* genus form intracellular Ca-carbonates and it has long been thought that this biomineralization process was specific to this bacterial taxon. However, widespread and phylogenetically diverse cyanobacteria have been shown to be able to biomineralize intracellular Ca-carbonates as well (Benzerara et al., 2014; Couradeau et al., 2012). Li et al. (2016) showed that the intracellular Ca-carbonates are amorphous calcium carbonates (ACC) in all these cyanobacteria. Moreover, a magnetotactic bacterium affiliated to Alphaproteobacteria was recently shown to biomineralize intracellular ACC as well (Monteil et al., 2020). Last, many eukaryotes have also been shown to biomineralize ACC instead of crystalline calcite or aragonite, at least as a precursor phase (Addadi et al 2003). Whether this capability to form intracellular $CaCO_3$ convergently appeared several times during evolution in these organisms or it involves homologous pathways (in connection with e.g., C fixation) remains to be determined by future molecular biology approaches.

There are discrepancies in the literature about the nature of the intracellular Ca-carbonates in *Achromatium* (Table S1). These discrepancies started as early as *Achromatium* was discovered. Indeed, Schewiakoff (1893) followed by, e.g., Virieux (1913) first suggested that intracellular granules were composed of calcium oxalate. This interpretation was based on the observation of recrystallized granules extracted from *Achromatium* cells by various reactants, which looked like the Ca-oxalates formed by plants. However, a few years later, West and Griffiths (1913),

also using various chemical tests, concluded that the granules were calcium carbonates. At that time, they thought that they were analyzing cells belonging to a genus different from the one analyzed by Schewiakoff (1893), which they named *Hillhousia viirabilis*, but it was later shown to be *Achromatium* as well. Moreover, West and Griffiths (1913) mentioned that the $CaCO_3$ granules in the cells did not polarize and only crystallized when extracted from the cells. They therefore concluded that the calcium carbonate granules within the cells were in "a colloidal form" and different from the ones in dead organisms. Bersa (1926) reiterated similar experiments and again suggested that *Achromatium* granules were composed of amorphous $CaCO_3$. However, we noticed that authors have started to mentioned calcite instead of amorphous $CaCO_3$ at least since 1991 (e.g., Babenzien, 1991). Head et al. (1995) and Head et al. (2000) directly addressed the question of the crystallinity of *Achromatium* $CaCO_3$ granules by performing x -ray diffraction analyses of purified preparations of intact cells and suggested that the granules were calcite and not another structural form. Interestingly, Gray (2006) mentioned calcite but specified that this calcite may not be purely crystalline. More recently, Salman et al. (2015) analyzed Ca-carbonate granules *in situ* within *Achromatium* cells by Raman microspectroscopy and also concluded that they were calcite crystals. Consistently, most recent studies assumed that intracellular granules were calcite crystals based on the latest reports in the literature (e.g., Babenzien et al., 2015; Ionescu et al., 2017; Mansor et al., 2015; Schorn & Cypionka, 2018; Yang et al., 2019). Yet, the observations by West and Griffiths (1913) suggesting that *Achromatium* $CaCO_3$ granules are composed of ACC seem precisely documented. Moreover, the presence of intracellular ACC in cyanobacteria and the recently discovered magnetotactic alphaproteobacterium urges new efforts in characterizing the crystallinity of $CaCO_3$ granules in *Achromatium*. If there was a difference between *Achromatium* and other bacteria, this would suggest that specific mechanisms are involved in *Achromatium* and other bacteria in order to crystallize Ca-carbonate or preserve ACC from

crystallization and they would need to be investigated in the future. Moreover, since ACC and calcite have different thermodynamic properties, they may hold different functional roles and/or the same role but with different efficiencies. Consequently, we re-investigated the nature of the $CaCO_3$ granules in *Achromatium* cells by conducting Raman analyses on *Achromatium* populations found in the sediments of Lake Pavin.

2. Material & Methods

2.1 Site description and sample collection

Sediments were collected on the shore of Lake Pavin, Massif Central, France in November 2019. Sampling was achieved by filling one-litre glass bottles with 300-400 mL of sediments and 600-700 mL of water that overlaid the sediments. Air bubbles were excluded. Once in the laboratory, bottles were stored with their cap closed, under dim light and at room temperature (~25°C) from a few days up to a few months. The sampling location at Lake Pavin was 45.499107°N, 2.886273°E. No *in situ* measurement of O_2, sulfate and sulphide profiles was conducted on these samples. However, a previous study showed that the oxic-anoxic boundary extended in the first five millimetres of the sediments (Monteil et al., 2020).

2.2 Light microscopy observations, cell sorting and whole genome amplification (WGA)

Observation and micromanipulation were carried out on a 20-µL drop of pore water harvested in the first millimetre below the interface water/sediments of a sample collected in Lake Pavin. Cell sorting was done with an InjectMan® NI2 micromanipulator and a CellTram® vario, hydraulic, manual microinjector from Eppendorf mounted on a Leica DM IL LED microscope equipped with a 63x/0.70 PH objective. The microscope and micromanipulator were placed inside a clean chamber exposed beforehand for 1 h to ultraviolet germicidal irradiation (wavelength of the lamp: 254 nm). Single-cells with an ultrastructure and granules typical of

189 *Achromatium* species were transferred two consecutive times with a sterile microcapillary into
190 a 4-µL drop of Lake Pavin water filtered at 0.2 µm, before their final transfer into a 4-µL drop
191 of phosphate buffer saline (PBS). This drop was stored at -20°C before WGA. To obtain
192 sufficient gDNA for 16S rRNA gene sequencing, WGA was carried out using the multiple
193 displacement amplification (MDA) technique with the REPLI-g Single-Cell Kit (QIAGEN)
194 following the manufacturer's instructions.
195
196 **2.3 Cloning and sequencing of the 16S rRNA genes**
197 The 16S rRNA gene was amplified using the Phusion® Hot Start Flex DNA Polymerase
198 following the manufacturer's recommendations, a DNA template of 50 - 70 ng/µl and the 27F
199 5'-AGAGTTTGATCMTGGCTCAG-3' and 1492R 5'-TACGGHTACCTTGTTACGACTT-
200 3' primers (Lane, 1991). Blunt-end fragments of 16S rRNA gene sequences were cloned using
201 a Zero Blunt® TOPO® PCR Cloning Kit with One Shot® TOP10 chemically competent *E. coli*
202 cells. The inserts were sent for sequencing (Eurofins Genomics Germany GmbH). Sequences
203 were compared to data found in the NCBI nucleotide database using the Basic Local Alignment
204 Search Tool. Sequences were deposited in the NCBI Genbank database under the accession
205 numbers MN990460 and MN990461.
206
207 **2.4 Phylogenetic analyses**
208 The 16S rRNA gene sequences of representative type strains of all Thiotrichales
209 (Gammaproteobacteria) families were downloaded from the public NCBI database (January
210 2020). This database was enriched with several sequences related to the *Achromatium* genus,
211 some of the newly described candidate Thiotrichales species and the sequences of the two Lake
212 Pavin $CaCO_3$-accumulating OTUs (Pavin-1 and Pavin-2). The 52 sequences were aligned using
213 MAFFT 7 (Katoh & Standley, 2013) and trimmed using Gblocks (Talavera & Castresana, 2007)
214 to get a final alignment of 1410 bp. A maximum- likelihood (ML) tree was built with RAxML

8.2.6 (Stamatakis, 2014) under the GAMMAI model of rate heterogeneity and the GTR substitution model. A total of 350 bootstrap replicates automatically determined by the MRE-based bootstopping criterion were conducted using the rapid bootstrapping algorithm, among which 100 were sampled to generate proportional support values. In this phylogeny, members of the Francisellaceae and Fastidiosibacteraceae families were used to root the tree based on previous phylogenies of the Thiotrichales order (Xiao et al., 2018).

2.5 Preparation of cells for microscopy analyses

Lake Pavin *Achromatium* cells were sorted by micromanipulation and directly deposited on a glass coverslip (18 x 18 mm) coated with poly-L-lysine to improve cells' adhesion. Raman microspectroscopy analyses were conducted first with a systematic localization of the analyzed cells. The coverslip was then sputtered with carbon. Cells analyzed by Raman were relocated and further analyzed by scanning electron microscopy (SEM). We note that the assessment of $CaCO_3$ crystallinity was performed by Raman spectroscopy before C-sputtering and therefore we presently do not know if the later step may induce ACC crystallization. Moreover, air-drying of cells, exposition of cells to vacuum and C-sputtering can cause cell damages, in particular flattening. However, in the present study only the features that were not affected (such as presence/absence of a cell wall) were investigated.

2.6 Reference ACC synthesis and thermogravimetric analyses

ACC synthesis was carried out following the procedure described by Wang et al. (H.-W. Wang et al., 2017). Fresh solutions of 100 ml of 50 mM $CaCl_2$ and 50 mM Na_2CO_3 (+ 0.5 g NaOH) were prepared with cold (4˚C) MilliQ water. The $CaCl_2$ solution was placed in a 500 mL Teflon centrifuge bottle. A 30 x 30 cm^2, 75 mm thick polyethylene sheet was placed in the upper part of the centrifuge bottle with a steel ball (1 cm in diameter, 5 g). The Na_2CO_3-NaOH solution was poured into the polyethylene sheet, keeping both solutions separated. The bottle was then

placed in a centrifuge (Beckman Coulter model Avanti J-20 XP) pre-cooled to 4 ˚C, and it was spun at 4000 rpm for 3 minutes. The force exerted by the ball on the polyethylene sheet breaks the sheet and throws the Na_2CO_3–NaOH solution into the $CaCl_2$ solution extremely rapidly. The supernatant liquid was poured out and the solid was rinsed with a few mL of dry cold (4˚C) acetone. The suspension in acetone was filtered on a Buechner funnel, the solid was recovered and dried at room temperature under vacuum for 4-5 h.

Thermogravimetric analysis-differential scanning calorimetry (TGA-DSC) analyses of the reference ACC were performed using a METTLER TOLEDO® TGA/DSC3+. 8.6 mg of dry powdered sample were placed in an alumina crucible and the sample was heated from 25 to 750°C under a 20mL/min N_2 flow. The temperature scanning rate was set at 20°C per minute. Noteworthy, TGA-DSC analyses could not be performed on natural samples due to limited amounts of sample.

2.7 Raman microspectroscopy analyses

Raman spectra were recorded using a Renishaw InVia Reflex spectrometer equipped with a 532 nm Renishaw diode laser. The laser was focused on the sample using a DM2500 Leica microscope with a 100× objective (NA= 0.75) to obtain a planar resolution of ~ 1 μm^2. The maximum laser power was measured at ~90 mW under the microscope without the objective. The laser incident beam was polarized circularly by a quarter wavelength plate placed before the microscope. We selected several neutral density filters to acquire Raman spectra at varying laser powers from 0.1 up to 100% of the maximum laser power. Therefore, at 1%, the power delivered in a 1 μm^2 spot was 900 μW and the irradiance was 9.10^8 $W.m^{-2}$. The signal was filtered by edge filters and dispersed by a diffraction grating with 2400 grooves/mm and the signal was analyzed with a RENCAM CCD (charge-coupled device) detector. Before each

session, the spectrometer was calibrated in energy using a silicon standard. Spectra were collected using the software WIRE 4.3 provided by Renishaw.

It has been shown that Raman spectra of the different $CaCO_3$ crystalline polymorphs (calcite, aragonite, vaterite) are significantly different from each other and can therefore be used as unambiguous signatures of these phases (Behrens et al., 1995). The ν_1 Raman bands of ACC and calcite were fitted with 2 Voigt functions using the FitViewer program, a Graphical User Interface (GUI) designed by Olivier Forni and Paolo Pilleri at the Institut de Recherche en Astrophysique et Planétologie (IRAP). The fit was performed with the MPFIT algorithm (Markwardt, 2009) which is based on the Levenberg-Marquardt method (Moré, 1978). As further described by (Váczi, 2014), the profile described by the Voigt function results from the convolution of a Lorentzian profile by a Gaussian function. A Gaussian profile was assumed to model the instrumental contribution and its FWHM was fixed at 1.9 cm^{-1}, equal to the spectrometer bandpass as measured experimentally using the emission band of a Ne lamp. In turn, the Lorentzian function is assumed to model the Raman transitions, corrected from the instrumental response.

2.8 Scanning Electron Microscopy

Scanning electron microscopy (SEM) analyses were performed using a Zeiss ultra 55 field emission gun SEM. Secondary electron (SE2) images were acquired using an Everhart Thornley detector at an accelerating voltage of 2.0 kV and a working distance of ~3.5 mm. Backscattered electron images were acquired for chemical mapping using an angle selective backscattered (AsB) detector at an accelerating voltage of 15 kV and a working distance of ~7.5 mm. Elemental maps were generated from hyperspectral images (HyperMap) by energy dispersive X-ray spectrometry (EDXS) using an EDS QUANTAX detector. EDXS data were analyzed using the ESPRIT software package (Bruker).

3. Results

Some pore water harvested from the first millimetres below the water/sediment interface was deposited on a glass slide and examined under the light microscope. Large cells were observed, measuring on average 22.3± 6.7 µm in length and 14.2± 4.0 µm in width (31 measurements), which corresponded to volumes between ~500 and 3000 µm^3 (Figure 1). They contained numerous intracellular inclusions measuring around 3±1.3 µm in diameter (18 measurements, 4 cells). Five cells were sorted and the 16S rRNA gene of two of them was successfully sequenced after whole genome amplification. Their 16S rRNA gene sequences clustered in the *Achromatium* cluster A (Figure 2) as defined by Mansor et al. (2015). They shared 96 to 97% sequence identity with the *Achromatium* L79966 and AF129550 OTUs, sequenced from a wetland on the margins of Rydal Water and an upland tam on Jenny Dam, respectively, both located in the United Kingdom and composed of freshwater as in Lake Pavin (Gray et al., 1999). Moreover, *Achromatium* cells in Lake Pavin had a size range consistent with that of *Achromatium* cells previously observed in Rydal water (cell volumes between 1000 and 30,000 µm^3) and the Jenny Dam (cell volumes between 150 and 26,000 µm^3).

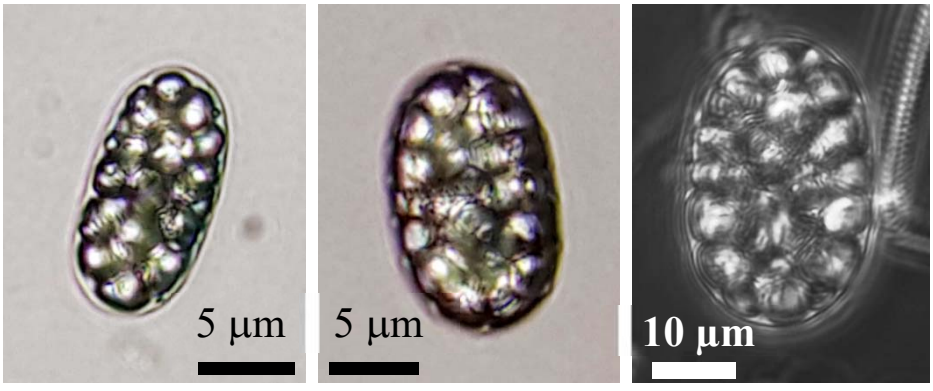

Figure 1: Light microscopy images of *Achromatium* cells isolated from Lake Pavin sediments**.**

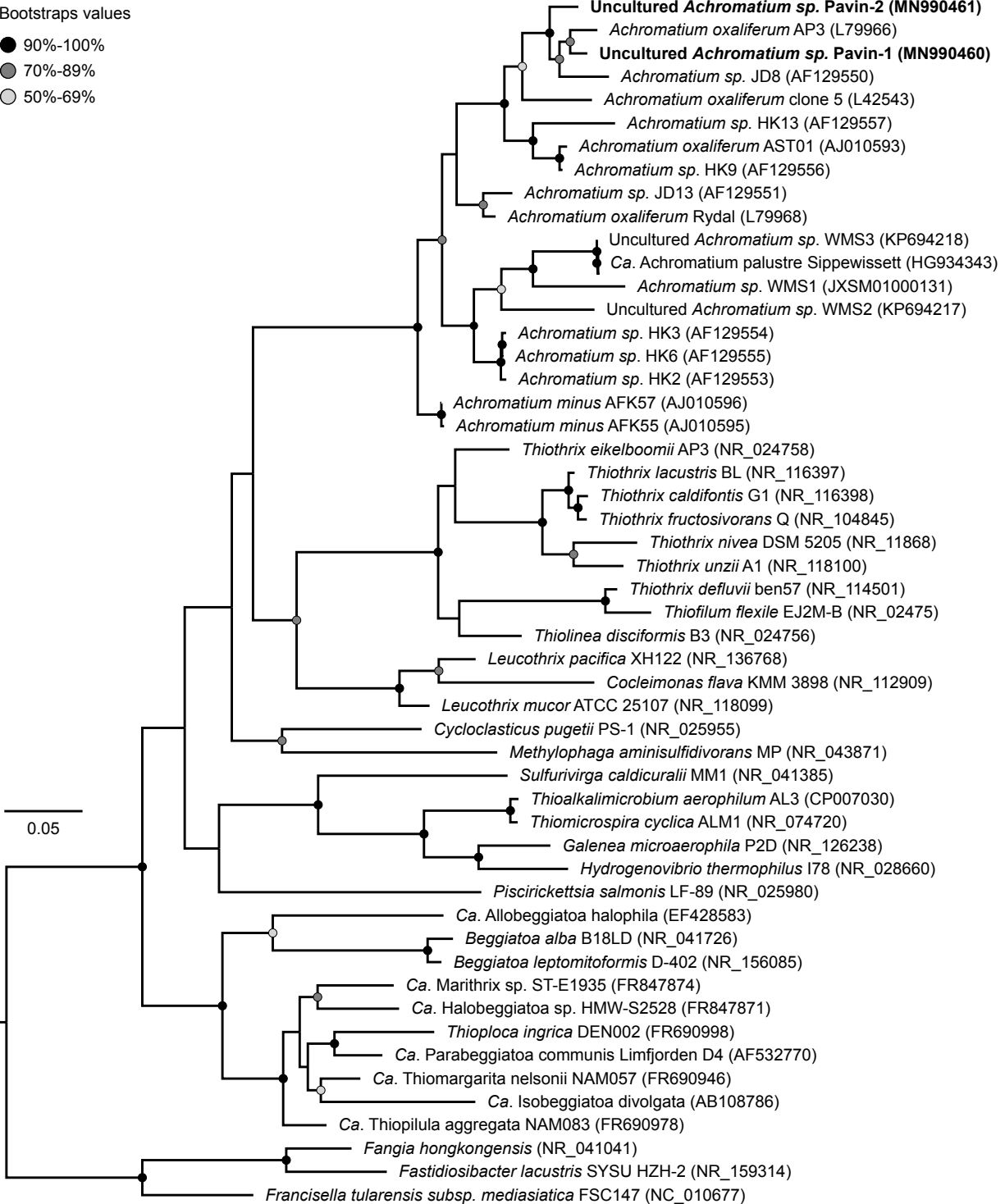
Bootstraps values
90%-100%
70%-89%
50%-69%
0.05
Uncultured Achromatium sp. Pavin-2 (MN990461)
Achromatium oxaliferum AP3 (L79966)
Uncultured Achromatium sp. Pavin-1 (MN990460)
Achromatium sp. JD8 (AF129550)
Achromatium oxaliferum clone 5 (L42543)
Achromatium sp. HK13 (AF129557)
Achromatium oxaliferum AST01 (AJ010593)
Achromatium sp. HK9 (AF129556)
Achromatium sp. JD13 (AF129551)
Achromatium oxaliferum Rydal (L79968)
Uncultured Achromatium sp. WMS3 (KP694218)
Ca. Achromatium palustre Sippewissett (HG934343)
Achromatium sp. WMS1 (JXSM01000131)
Uncultured Achromatium sp. WMS2 (KP694217)
Achromatium sp. HK3 (AF129554)
Achromatium sp. HK6 (AF129555)
Achromatium sp. HK2 (AF129553)
Achromatium minus AFK57 (AJ010596)
Achromatium minus AFK55 (AJ010595)
Thiothrix eikelboomii AP3 (NR_024758)
Thiothrix lacustris BL (NR_116397)
Thiothrix caldifontis G1 (NR_116398)
Thiothrix fructosivorans Q (NR_104845)
Thiothrix nivea DSM 5205 (NR_11868)
Thiothrix unzii A1 (NR_118100)
Thiothrix defluvii ben57 (NR_114501)
Thiofilum flexile EJ2M-B (NR_02475)
Thiolinea disciformis B3 (NR_024756)
Leucothrix pacifica XH122 (NR_136768)
Cocleimonas flava KMM 3898 (NR_112909)
Leucothrix mucor ATCC 25107 (NR_118099)
Cycloclasticus pugetii PS-1 (NR_025955)
Methylophaga aminisulfidivorans MP (NR_043871)
Sulfurivirga caldicuralii MM1 (NR_041385)
Thioalkalimicrobium aerophilum AL3 (CP007030)
Thiomicrospira cyclica ALM1 (NR_074720)
Galenea microaerophila P2D (NR_126238)
Hydrogenovibrio thermophilus I78 (NR_028660)
Piscirickettsia salmonis LF-89 (NR_025980)
Ca. Allobeggiatoa halophila (EF428583)
Beggiatoa alba B18LD (NR_041726)
Beggiatoa leptomitoformis D-402 (NR_156085)
Ca. Marithrix sp. ST-E1935 (FR847874)
Ca. Halobeggiatoa sp. HMW-S2528 (FR847871)
Thioploca ingrica DEN002 (FR690998)
Ca. Parabeggiatoa communis Limfjorden D4 (AF532770)
Ca. Thiomargarita nelsonii NAM057 (FR690946)
Ca. Isobeggiatoa divolgata (AB108786)
Ca. Thiopilula aggregata NAM083 (FR690978)
Fangia hongkongensis (NR_041041)
Fastidiosibacter lacustris SYSU HZH-2 (NR_159314)
Francisella tularensis subsp. mediasiatica FSC147 (NC_010677)

Figure 2: Maximum likelihood phylogenetic tree of the Thiotrichaceae and Piscicettsiaceae families based on the 16S rRNA gene sequences showing the evolutionary relationships between the two $CaCO_3$-accumulating isolates from Lake Pavin (Pavin-1 and Pavin-2) and their *Achromatium* relatives. The tree was built with the maximum likelihood method and the GTRGAMMAI substitution model. *Fangia hongkongensis*, *Fastidiosibacter lacustris* and *Francisella tularensis* subsp. mediasiatica were used as an outgroup. The tree was drawn to scale and branches length represents the number of base substitutions per site. Only bootstrap values above 50% are shown and annotated to a circle.

Raman spectroscopy analyses were conducted on seven *Achromatium* cells sorted from the sediments by micromanipulation. Several spots were analyzed for each cell. Then, cells were systematically relocated and imaged by SEM and their elemental chemical composition mapped by SEM-EDXS.

One of the 7 cells showed a particular Raman spectrum with major peaks at 150.8, 219.7 and 473.5 cm^{-1} (Figure 3). This spectrum was identical to the spectrum referred to as biosulfur by Nims et al. (2019), consisting of elemental sulfur inclusions in bacteria. Consistently with what was reported by these authors, the three observed peaks were unambiguously assigned to asymmetric S-S bending, symmetric S-S bending and S-S bond stretching of a S_8 ring structure, respectively. Consistently, SEM-EDXS mapping showed that this cell contained numerous S-rich inclusions (Fig. S1).

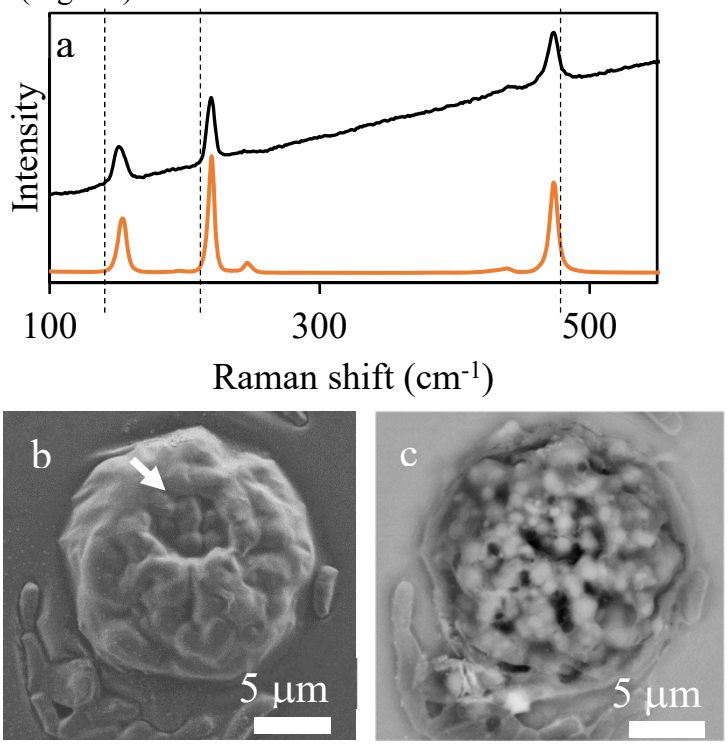

Figure 3: (a) Raman spectrum of an *Achromatium* cell with sulfur inclusions. The top black spectrum is obtained on the *Achromatium* cell shown in the SEM images. The bottom orange spectrum was issued from the RUFF database and was measured on elemental sulfur (#R040135). Vertical dashed lines indicate peaks at 150.8, 219.7 and 473.5 cm^{-1}. (b) SEM image of the analyzed *Achromatium* cell were measured in the secondary electron mode (SE2; left) with an accelerating voltage of 2 keV. The white arrow indicates the approximate location where a low power Raman analysis was performed. (c) SEM image of the same cell shown in (b), observed in the backscattered electron mode (ASB; right) with an accelerating voltage of 15 keV.

On 5 cells out of 7, Raman spectra measured with 1% of the maximum laser power were similar to those shown in Figure 4. These spectra showed two sets of peaks: a first set comprised four peaks at 604, 749.4, 1128 and 1311.3 cm^{-1}. Based on Pätzold et al. (2008), these peaks were assigned to the ν_{24}, ν_{15}, ν_{22} and ν_{21} modes of a porphyrin ring in cytochromes. Interestingly, these bands disappeared upon prolonged irradiation (Fig. S2). The second set comprised a very broad peak, likely the convolution of two broad peaks, extending between 681 and 752 cm^{-1} and another broad peak centered, depending on the spectra, between 1079.45 and 1082.43 cm^{-1}. These peaks were identical to those of an amorphous calcium carbonate (ACC) reference spectrum (Figure 4). The very broad band between 681 and 752 cm^{-1} was assigned to the in-plane bend (ν_4) of C-O bonds. The strong and broad peak at around 1079.9 cm^{-1} corresponded to the symmetric stretching of C–O bonds in carbonate groups (ν_1 peak) in a $CaCO_3$ phase. This assignment to ACC was further supported by the absence of sharp peaks characteristic of lattice mode vibrations in crystalline $CaCO_3$ phases below 400 cm^{-1}. Instead, we observed a single broad bump between the cutoff at ~50 nm and ~400 nm (Figure 4). Accordingly, SEM-EDXS analyses showed that these cells were rich in Ca with a minor EDXS peak of Mg, the relative height of which varied from one cell to another (Fig. S1).

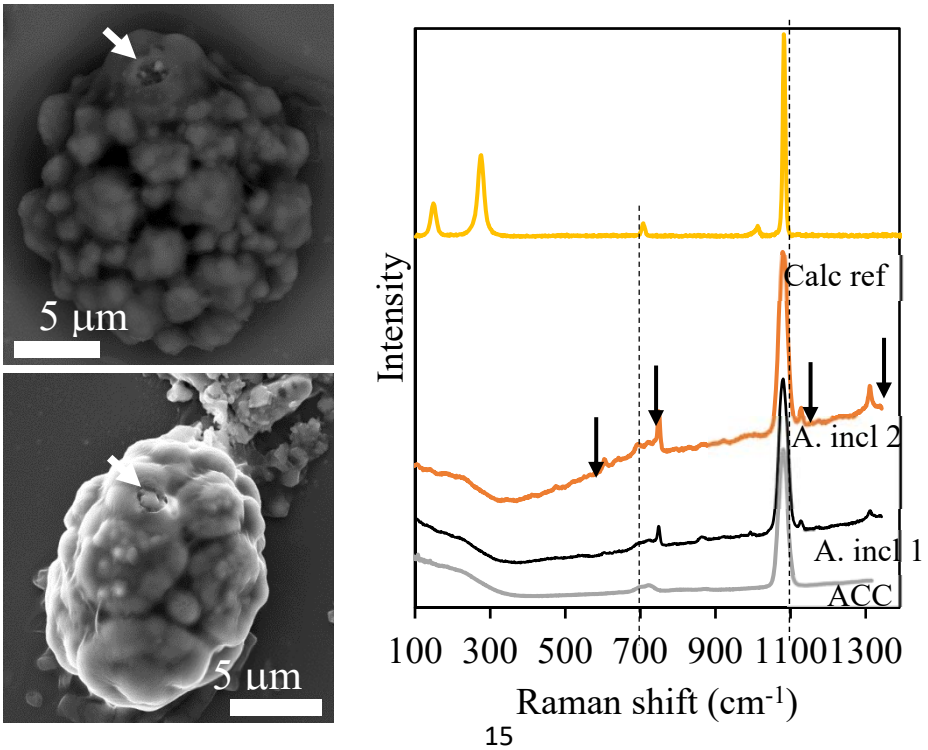

Figure 4: (Left) SEM images of the cells on which the Raman spectra were measured. White arrows indicate where full power Raman analyses were performed. (Right) Raman spectra. The two middle spectra (A. incl 1 and 2) are Raman spectra of $CaCO_3$ inclusions in *Achromatium* cells. The two dashed lines show (i) a broad band between 681 and 752 cm^{-1}, assigned to the in-plane bend (ν_4) of C-O bonds in ACC and (ii) a broad band around 1079.9 cm^{-1} assigned to the symmetric stretching (ν_1) of C–O bonds in carbonate groups in ACC. Arrows show bands at 604.2, 749.4, 1127.9 and 1311.3 cm^{-1}, assigned to the ν_{24}, ν_{15}, ν_{22} and ν_{21} modes of a porphyrin ring in cytochromes. The top spectrum (Calc ref) is a Raman spectrum of a reference calcite crystal retrieved from the RUFF database (#R040170). The bottom spectrum (ACC ref) is a Raman spectrum of a synthetic reference ACC particle.

When full laser power was used, the spectra measured on *Achromatium* intracellular granules changed and eventually showed very different spectral features (Figure 5 and Figure 6). First, two Raman bands appeared at ~154 and 280 cm^{-1} after irradiation. These bands were unambiguously assigned to the translation and higher frequency libration modes in calcite and were due to collective synchronized vibrations of atoms around their equilibrium positions (Perrin et al., 2016). The very broad ν_4 band of ACC was replaced by a narrow band at 712.2 cm^{-1} that was consistently assigned to the ν_4 mode of calcite. The broad band at ~1079.9 cm^{-1} of ACC was replaced by a narrower band at ~1086 cm^{-1}, also consistently assigned to ν_1 in calcite. Last, the Raman bands at 604, 749.4, 1128 and 1311.3 cm^{-1} of cytochromes, associated with ACC, were absent from the calcite spectra. SEM pictures at low voltage of the cells where this transformation was observed showed that they were systematically enveloped by a cell wall, detected here as an envelope opaque to low energy electrons and therefore preventing the direct visualization of the granules inside the cells (Figures 4-6). In contrast, when the cell wall was disrupted, one could visualize directly the intracellular $CaCO_3$ granules, as shown in Figure 6. Local damages induced by the laser spot could be observed as a crater measuring ~2 μm in diameter (Figure 5b). In one case, the cell partly disrupted and the irradiated calcite residue was extruded from the cell. The resulting byproduct showed a granular microtexture (Figure 6).

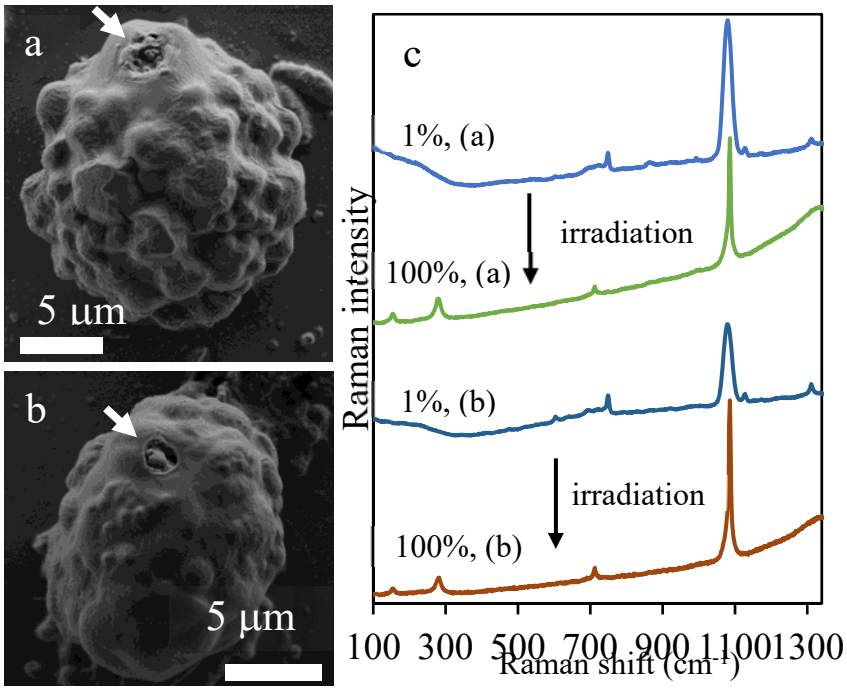

Figure 5: (a) and (b) SEM images acquired at 2 keV in the secondary electron mode showing the *Achromatium* cells analyzed by both Raman and SEM. Arrows show the irradiation spots where ACC transformed into calcite following full laser power irradiation. (c): Raman spectra obtained using 1% and 100% laser power on cells shown in (a) and (b). Dashed lines are located at ~154, 280, 604, 712.2, 749.4, 1079.9, 1127.9 and 1311.3 cm^{-1}.

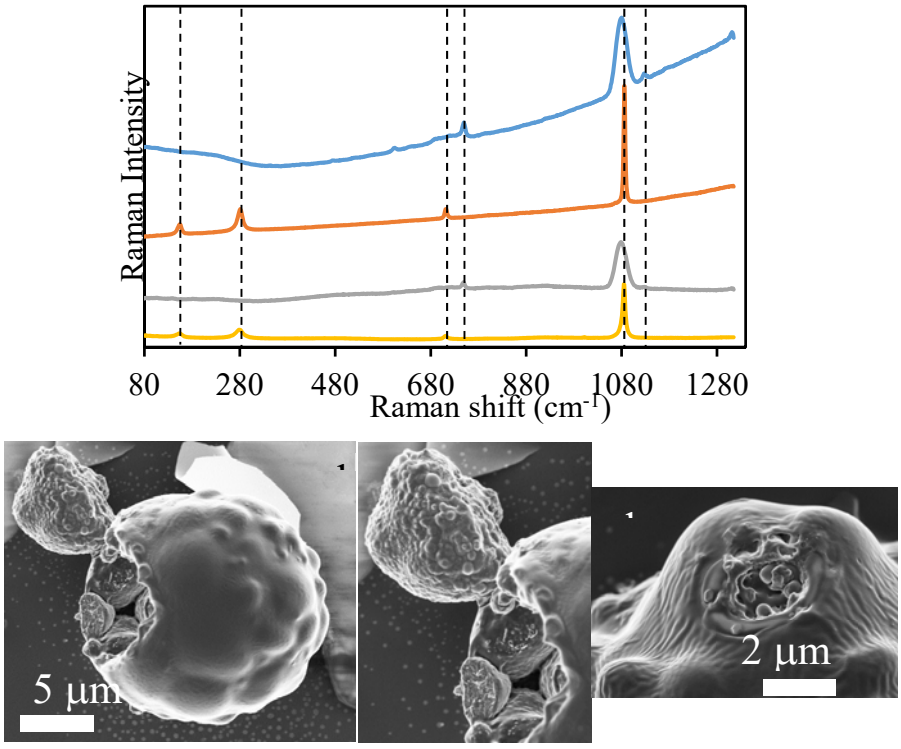

Figure 6: (a) Raman spectra of ACC granules in 2 *Achromatium* cells obtained by low laser power irradiation (blue and grey spectra), before transformation into calcite after full laser power irradiation (orange and yellow). Dashed vertical lines are located at ~154, 280, 712.2, 749.4, 1079.9, and 1127.9 cm^{-1}. (b) SEM image obtained at 2 keV by the InLens detector. A fragment was partly detached from the cell on the top left after laser irradiation. (c) Close-up

of the detached fragment showing the granular texture of calcite in the extruded fragment *vs* smooth texture in ACC within the cells. (d) Close-up of the crater induced by laser in another *Achromatium* cell and showing the texture of the transformed area.

The ν_1 band of *Achromatium* $CaCO_3$ granules irradiated at low laser power (from 1 to 10% of the total power) and full laser power were systematically fitted. In most cases, a very good fit was obtained using one Voigt function but for several spectra measured after strong irradiation, the ν_1 band was clearly asymmetric and best fitted with two Voigt functions (Fig. S3). When plotting the ν_1 band position *vs* the full width at half maximum (FWHM) of the Lorentzian profile, a clear difference was observed between weakly (0.1-10% of the maximum laser power) *vs* strongly (100% of the maximum laser power) irradiated granules, further highlighting the transformation of ACC into calcite upon irradiation (Figure 7). The FWHM for weakly irradiated synthetic and *Achromatium* ACC varied between 24.9 and 28.6 cm^{-1} and was positively correlated with the band position, which varied between ~1079.5 and 1082.4 cm^{-1}. In contrast, the FWHM for all strongly irradiated *Achromatium* ACC were between 24.7 down to 2.5 cm^{-1} which negatively correlated with the band positions, varying between 1082.4 and 1086.3 cm^{-1}. The components with higher FWHM/lower position were minor fit components of asymmetric bands and were interpreted as poorly crystalline remnants mixed with more crystalline components in irradiated zones similarly to what was shown by Wehmeister et al. (2011) (Figure 7).

In the case of one *Achromatium* cell, the Raman spectrum measured with 1% of the maximum laser power was very similar to that of the most irradiated *Achromatium* granules and to that of calcite with bands at ~154, 280, 712.2 and 1086.2 cm^{-1} (Figure 8). SEM observations performed at low voltage showed that this cell was devoid of a cell wall on the contrary to the cells containing ACC as mentioned before.

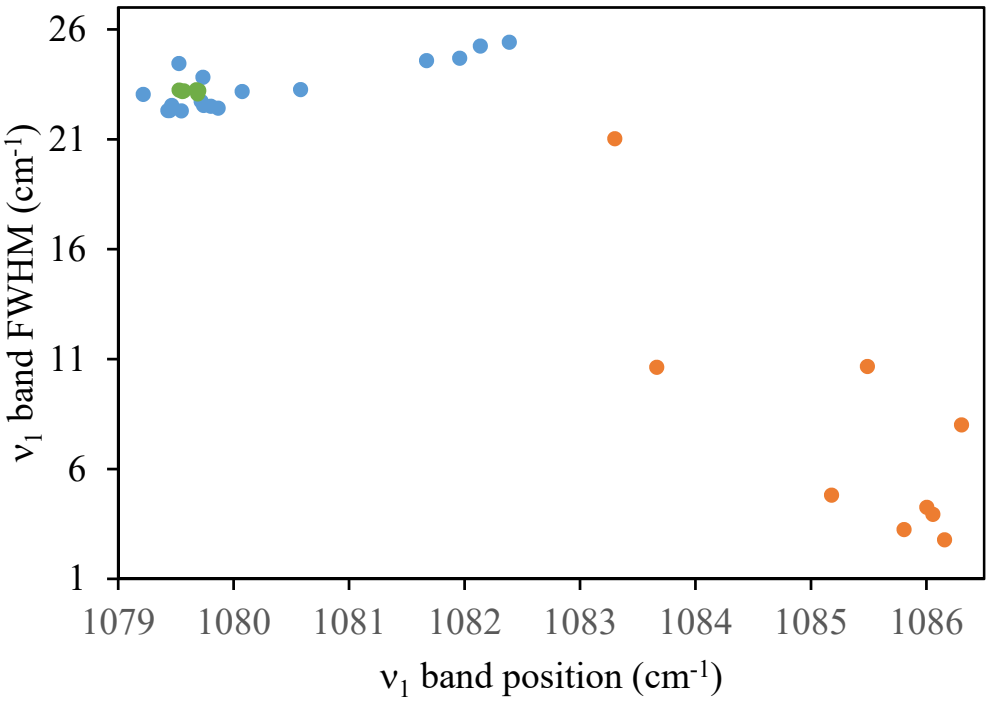

Figure 7: Scatterplot showing the full width at half maximum (FWHM) versus the position for the ν_1 Raman band of the $CaCO_3$ phase. Blue dots correspond to Raman spectra measured on *Achromatium* $CaCO_3$ inclusions with reduced laser power (1 or 5 %). Green dots correspond to Raman spectra measured on synthetic reference ACC grains with reduced laser power (1 or 5 %). Orange dots correspond to Raman spectra measured on *Achromatium* $CaCO_3$ inclusions with full laser power and showing signs of crystallization.

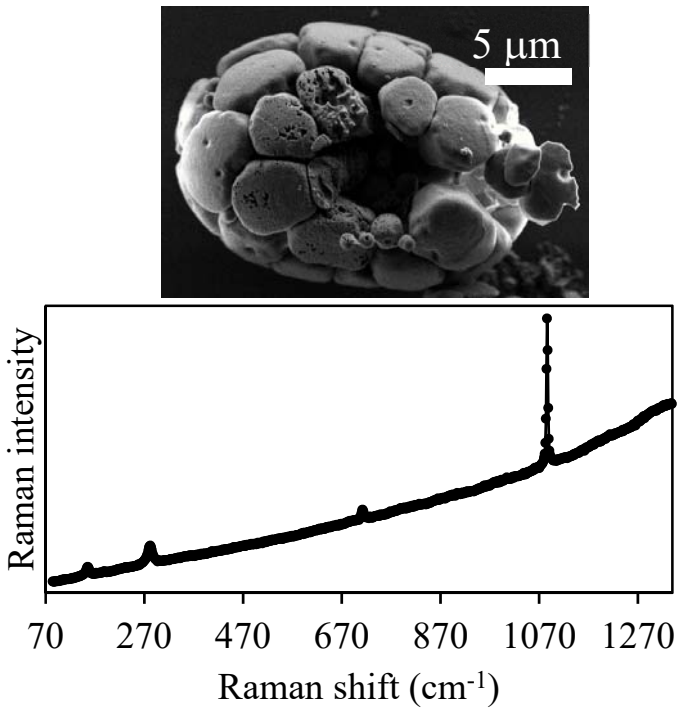

Figure 8: (a) SEM images acquired at 2 keV in the secondary electron mode showing an *Achromatium* cell analyzed by both Raman at 1% laser power and SEM. (b): Raman spectrum obtained using 1% laser power on the cell shown in (a). Dashed lines are located at ~154, 280, 712.2 and 1086.2 cm^{-1} and underline bands that are characteristic of calcite.

4. Discussion

4.1. Precautions to be taken in order to assess the crystallinity of $CaCO_3$ in *Achromatium* cells

The present data clearly show that the $CaCO_3$ granules in Lake Pavin *Achromatium* intact cells are composed of ACC and not calcite. Only one cell contained calcite granules but SEM observations suggested that this cell was damaged since it did not show any cell wall as discussed below. Several studies have detailed how Raman spectroscopy could unambiguously discriminate between ACC and calcite (e.g., DeCarlo, 2018). This includes the presence (in calcite)/absence (in ACC) of lattice modes at ~154 and 280 cm^{-1}; a sharp (calcite) *vs* wide (ACC) ν_1 peak. The latter feature has been explained as the result of a high variability in the bonding environment around the carbonates in ACC which causes deviations in the lengths of C–O bonds. Last, a shift in the ν_1 peak position from lower (ACC) to higher (calcite) wavenumbers is observed. Wang et al. (2012) and Perrin et al. (2016) showed that variations in the Mg content of ACC and calcite could change in a correlated manner with the FWHM and position of the ν_1 peak. Accordingly, we observed in our study some correlated variations in the FWHM and peak position of the ν_1 peak in ACC granules, with variation of FWHM in the 22.5-25.4 cm^{-1} range, which according to Wang et al. (2012) may be explained by variations in their Mg contents in the 0-10% range. Perrin et al. (2016) also noticed that (1) the FWHM of calcite and ACC, whatever their Mg content, did not overlap, and (2) ν_1 wavenumbers lower than 1086 cm^{-1} and ν_1 FWHM greater than 22 cm^{-1} were two unambiguous criteria to determine the amorphous nature of calcium carbonate. Therefore, it can be confidently concluded that Raman spectra collected on most Lake Pavin *Achromatium* cells were characteristic of ACC.

This conclusion fully agrees with the early studies by West and Griffiths (1913) who suggested that intracellular granules in *Achromatium* were composed of a colloidal form of $CaCO_3$ and

538 later on by Bersa (1926) who mentioned amorphous $CaCO_3$ ("amorphen (kolloidalen) Form"
539 in their manuscript). It also better explains Yang et al. (2019)'s FIB observations of composite
540 structure of the granules with submicrometer laminations, which would be difficult to explain
541 within a single crystal, as mentioned by the authors themselves. Similar laminations in ACC
542 granules, attributed to chemical variations, were observed by TEM by Martignier et al. (2017)
543 (2017) and Cam et al. (2016).
544 We note that several artefacts may lead to an erroneous assessment of the crystallinity of
545 *Achromatium* $CaCO_3$ granules. First, in a population of *Achromatium* cells, some ACC granules
546 may transform into calcite because of, e.g., cell death and/or sample preparation. Indeed, it has
547 been emphasized by many authors (e.g., Gower, 2008; Politi et al., 2006) that ACC is usually
548 unstable and often converts to a crystalline phase during sample preparation of biominerals for
549 *ex vivo* examinations. Consistently, a spontaneous transformation of ACC into calcite was
550 documented by the early observations by West and Griffiths (1913) and Bersa (1926) when
551 they killed the cells by adding alcohol or drying. Schorn et al. (2020) observed dissolution of
552 *Achromatium* ACC granules when they treated cells with acids. In the meantime, Schorn et al.
553 (2020) sometimes evidenced some crystallization when killing them with no acidification of
554 the solution. In the present study, while we observed that simple drying does not induce
555 crystallization of ACC, we observed one cell containing calcite. On the contrary to other cells,
556 this one lacked a cell wall. We cannot affirm whether the cell wall was already disrupted in the
557 sample before micromanipulation or if it occurred upon sample preparation but as mentioned
558 above, this explains why ACC granules transformed into calcite in this cell before Raman
559 analyses.
560 Second, in addition to sample preparation, irradiation at too high laser power can also cause
561 ACC crystallization as shown in the present study. This transformation may result from the
562 local heating of ACC in the laser spot over ~330°C, a temperature at which the solid-solid

563 transformation of ACC into calcite is detected by thermogravimetric analyses (Fig. S4). Such a
564 local increase of T may result from a high absorption of light by, e.g., cytochromes, which
565 contribute to the Raman signal of *Achromatium* cells and efficiently absorb visible light at ~530
566 nm (Okada et al., 2012) and a slow dissipation of the heat in the material (Fau et al., 2019). As
567 shown by Fau et al. (2019), a more precise assessment of the temperature increase induced by
568 laser heating would require the knowledge of the optical penetration depth and thermal
569 penetration depth in organics-containing ACC granules, which we do not know yet.
570 An alternative interpretation of these observations could consist in suggesting that only a
571 surficial layer of the *Achromatium* granules was illuminated and therefore heated by the laser.
572 This surficial layer would be an ACC layer covering an initially unseen calcite core. This
573 initially unseen calcite core may then become apparent after volatilization of the ACC layer.
574 However, this interpretation is unlikely for two reasons. First, this would mean that ACC is
575 quite opaque. While we do not know the value of the optical penetration depth as mentioned
576 above, Schmidt and Wagermeier (2017) reported that cystoliths in plants, composed of ACC
577 and measuring 40-60 μm function as light scatterers due to their transparency to visible light.
578 This suggests that green Raman light likely propagates throughout the 3-4 μm wide ACC
579 granules of *Achromatium*. Second, if a surficial layer of ACC was volatilized (after
580 crystallization into calcite at ~330°C), this would produce CaO, which we did not detect by
581 Raman.
582 Overall, the high susceptibility of ACC to transform into calcite upon cell death and/or sample
583 preparation and/or laser irradiation concurs to the assumption made by Gower (2008) that this
584 explains why it took so long to discover ACC although it is common. This applies well to
585 *Achromatium* too. Two studies produced data suggesting a calcitic nature of the $CaCO_3$ granules
586 in *Achromatium* using bulk x-ray diffraction (Head et al., 2000) and Raman spectroscopy
587 (Salman et al., 2015). However, XRD is much more sensitive to calcite than ACC and therefore

588 even in a bulk sample where most of the cells contain ACC and only a few dead ones contain
589 calcite, the latter signal would show up. Salman et al. (2015) analyzed *Achromatium* cells by
590 Raman spectroscopy and obtained one spectrum typical of calcite. However, they did not
591 mention the use of neutral density filters and may have acquired Raman spectra at full laser
592 power. Alternatively, morphologically and genetically distinct subpopulations of *Achromatium*
593 have been evidenced in several localities, although this idea was challenged by recent studies
594 that instead suggested variations in gene expression across varying environments (Ionescu et
595 al., 2020). One may postulate that some *Achromatium* populations may produce calcite instead
596 of ACC. Moreover, the *Achromatium* populations studied by Salman et al. (2015) thrived in a
597 salt marsh which is chemically very different from the freshwater of Lake Pavin. While it is not
598 clear how salinity may directly impact the stability of ACC, it is possible that environmentally-
599 driven variations in ion homeostasis in cells result in different chemical environments around
600 $CaCO_3$ granules. Similarly, one may wonder if *Achromatium minus* thriving in the more acidic
601 lake Fuchskuhle (pH=4.2-4.6) (Glöckner et al., 1999) may form calcite instead of ACC.
602 Overall, only future systematic studies will be able to decipher if intracellular $CaCO_3$ granules
603 in *Achromatium* living cells are always composed of ACC or sometimes calcite. The present
604 study offers guidelines to avoid potential artifacts including the use of low Raman laser
605 irradiation (preferably <1 mW for a 532 nm laser), then SEM to verify that the cell wall is still
606 enveloping the cells. It is possible that air-drying induces some damages in some cases and that
607 high-pressure freeze-substitution sample preparation may overcome this issue (Blondeau et al.,
608 2018) but this will have to be tested by future studies.

609 **4.2. What makes bacteria producing intracellular ACC instead of intracellular calcite?**
610

611 ACC are notoriously unstable phases (e.g., Addadi et al., 2003; Cavanaugh et al., 2019).
612 Therefore, it may appear surprising that *Achromatium*, a magnetotactic alphaproteobacterium
613 and cyanobacteria manage to preserve $CaCO_3$ as ACC intracellularly, and that it does not

transform into a crystalline phase such as calcite. In any case, the mechanism involved in this stabilization appears to no longer operate as soon as the cells lyse/die explaining why in this case ACC spontaneously crystallizes as reported here and by previous studies.

Laboratory biomimetic experiments showed that several chemical species can stabilize ACC at least transiently, such as magnesium ions, triphosphate ions, polymers such as diphosphate-substituted poly(ethylene glycol) and polyaspartate, polyphosphonates, some oligosaccharides or amino acids (Addadi et al., 2003; Zou et al., 2020). It is clear that at least some of these chemical species are abundant within the cell environment and may, therefore, play a role in ACC stabilization. However, how they may degrade and hence stop from stabilizing ACC when the cells disrupt remains to be understood. Alternatively, the stabilization of ACC may well be explained by confinement as demonstrated by, e.g. Zeng et al. (2018) and Cavanaugh et al. (2019). Based on microfluidics experiments, Cavanaugh et al. (2019) concluded that ACC is the expected byproduct of intracellular biomineralization occurring within a micrometer-sized compartment when the solution in this compartment is supersaturated with ACC. Moreover, they predict that ACC may remain stable for durations much longer than the lifetime of the organisms, i.e, months before crystallization occurs in 1% of 10 μm^3 vesicle and hundred years before it occurs in 99% of it. According to Jin et al. (2018), confinement can be seen as a barrier to water diffusion, which hinders the dissolution of ACC and reprecipitation as calcite. In cyanobacteria forming intracellular ACC, it has been shown that this confinement may be provided by an organic envelope of a yet-unknown composition (Blondeau et al., 2018). We presently do not know the genes or proteins involved in the formation of this organic envelope. In *Achromatium* and the recently discovered magnetotactic alphaproteobacterium, it has been suggested that ACC granules are confined by lipid bilayers (N. Gray & Head, 2014; Monteil et al., 2020). It can be speculated that such envelopes may also control the maximum size of the granules as observed for example n magnetotactic bacteria and prevent their agglomeration but

this will need further assessment in the future. Cavanaugh et al. (2019) noticed that when the confinement was broken, the exposition of ACC to heterogeneous nucleators induced rapid crystallization. Moreover, Liu et al. (2020) explained how this transformation of ACC into calcite by dissolution-reprecipitation could preserve the morphology of the granules by occurring without the need to nucleate a separate crystal. How the envelopes of ACC granules in cyanobacteria and *Achromatium* rupture will need to be further studied. For this purpose, TEM appears as the choice method since Raman microspectroscopy does not offer a spatial resolution high enough to detect such an organic envelope.

Overall, intracellular compartmentalization by lipid bilayers or proteins seems required to explain the formation and stabilization of ACC. This contradicts the recent suggestion by Schorn et al. (2020) that $CaCO_3$ in *Achromatium* cells would be in contact with the extracellular environment and form in pockets delimitated by an invagination of the cytoplasmic membrane and would, therefore, be periplasmic. We note that these conclusions by Schorn et al. (2020) were not derived from direct observations of the ACC granules within these pockets by, e.g. TEM tomography. Instead, they were postulated based on 1) the idea that the easy loss of $CaCO_3$ upon various physico-chemical treatments is consistent with the fact that they would not be membrane enclosed; and 2) the fact that fluorescein, a hydrophilic dye that does not penetrate membranes, did penetrate inside cavities hosting $CaCO_3$. However, several other facts may oppose Schorn et al. (2020) conclusion. First, ACC granules in cyanobacteria are also easily and rapidly lost upon various physico-chemical treatments and yet they clearly form within intracellular enclosed compartments (Blondeau et al., 2018). The chemicals used by Blondeau et al. (2018), i.e. ethanol which is membrane permeable, are not the same as those used by Schorn et al (2020), i.e. HCl, which is membrane impermeable. Yet both chemical may harm/stress the cells and induce intracellular changes. Second, Bentov et al. (2009) similarly observed that calcein, another membrane-impermeable dye as these authors underline it, did

664 stain the truly intracellular $CaCO_3$ of foraminifera. Last, the suggestion that $CaCO_3$ in
665 *Achromatium* would be in direct contact with the extracellular environment is inconsistent with
666 the report of ACC formation by some *Achromatium* cells in environmental solutions
667 undersaturated with ACC (Gray & Head, 2014).
668
669 **4.3. Implications of an ACC instead of a calcitic composition of intracellular granules**
670 There are several important ecological, geological and ultrastructural implications in reporting
671 that *Achromatium* intracellular granules are composed of ACC and not calcite.
672 First, several studies have discussed the potential function(s) of *Achromatium* $CaCO_3$ granules
673 (e.g., Gray & Head, 2014; Salman et al., 2015; Schorn et al., 2020; Yang et al., 2019). The
674 dominant view emerging lately suggests that these granules buffer intracellular pH, which may
675 otherwise vary due to the redox transformations of S species. It has been noted that for this
676 purpose the cells need to quickly adjust their $CaCO_3$ content to rapidly changing environmental
677 conditions, such as exposure to O_2 (Yang et al., 2019). We argue that this can be better explained
678 by ACC than calcite. Addadi et al (2003) and Weiner et al. (2005) consistently suggested that
679 ACC is a widespread biomineral phase and holds a homeostatic function in eukaryotes which
680 is facilitated by its metastability. Moreover, while the reactivity of calcite and ACC (e.g., the
681 kinetics of precipitation or dissolution) depends on prevailing chemical conditions, it has been
682 shown that under given conditions, ACC reactivity might be higher, partly because of a higher
683 surface area (Lassin et al., 2018). Altogether, these arguments support the idea that ACC may
684 respond more quickly to chemical changes than calcite and therefore fill such a buffering
685 function with a higher efficiency.
686 A second implication results from the solubility difference between ACC and calcite. Although
687 there remains some uncertainty about the exact value of the solubility of ACC, it is much higher,
688 at least one order of magnitude than that of calcite (Brečević & Nielsen, 1989; Carino et al.,

689 2017; Purgstaller et al., 2019). Solubility of ACC is even higher when its Mg content increases
690 (Purgstaller et al., 2019). This means that ACC precipitation requires a higher activity of Ca^{2+}
691 and/or a higher activity of HCO_3^- and/or a higher pH within the compartment where it forms. It
692 also means that ACC starts dissolving under conditions where calcite would still be stable. The
693 chemical composition inside the compartments where granules form is not known but future
694 modelling efforts aiming at inferring the chemical conditions prevailing in these compartments
695 should take into account the fact that these granules are composed of ACC and not calcite.
696 As a third implication, Bolze et al. (2002) reported densities of 1.62 and 2.75 g/cm^3 for hydrated
697 ACC and calcite, respectively. Fernandez-Martinez et al. (2013) measured a density of 2.18
698 g/cm^3 for dry ACC powder which remains significantly lower than that of calcite. This means
699 that when ACC crystallizes to calcite, this represents a volume variation between 20 to 40%.
700 This suggests that when ACC crystallizes to calcite in dying cells, one should expect a reduction
701 in size of the granules, unless further *post-mortem* crystal growth occurs. Moreover, it has been
702 hypothesized by some authors that intracellular granules in *Achromatium* are used to regulate
703 buoyancy of the cells (Gray, 2006). While ACC-filled cells remain denser than ACC free cells,
704 they are lighter than calcite-filled cells and therefore this role for increasing cell buoyant density
705 would be less efficient with ACC than calcite. Last, Mansor et al. (2015) noted that the
706 precipitation of $CaCO_3$ within cells generates H^+ and assumed that these protons may be used
707 to generate ATP. They used for their calculations the density of calcite to estimate the average
708 amount of Ca stored in cells which they equaled to the amount of CO_3^{2-} stored into the granules
709 and from there inferred the equivalent amount of generated protons. Here we note that these
710 calculations should be revised; using ACC density will decrease these numbers by at least 20
711 to 40%. We also note an additional difficulty for these calculations: first Mg substitution should
712 be taken into account since it impacts the density of the ACC phase. Then, on the contrary to
713 calcite, the $Ca:CO_3^{2-}$ stoichiometry is not always 1:1 in ACC as there can be some HCO_3^-

molecules as well, the proportion of which may depend on pH and temperature conditions (Carino et al., 2017). Those should not be counted to infer the equivalent proton amount. The advent of future experimental approaches e.g. measuring intracellular ATP *in vivo* will be essential to test these calculations.

Last, as mentioned above, the stability of ACC is lower than that of calcite. Therefore, even if ACC granules remain confined after the death of the cells, one may not expect to find genuine ACC in the geological record. Indeed, Cavanaugh et al (2019) showed that confined ACC granules measuring ~1 μm^3 would be preserved from crystallization up to about one million years. Therefore, a fossil of an ACC granule would be a crystalline phase, most likely calcite. In order to understand how to look for some potential traces of these ACC granules in the geological record, it will be important to decipher in the future: 1) what conditions are prone to crystallization of ACC in calcite; 2) if the morphology of ACC granules is always preserved upon crystallization; and 3) if the crystallized granules replacing ACC store some organic molecules that might be present in ACC granules and/or if a particular trace element composition is preserved.

5. Conclusion

We find robust evidence that cells of the giant gammaproteobacterium *Achromatium* sp. in Lake Pavin form intracellular ACC and not calcite. In contrast, previous reports of calcite may have been affected by the high instability of ACC, which transforms readily into calcite upon some sample treatments, which alter the integrity of the cells, or strong laser irradiation. Raman microspectroscopy seems to be the most appropriate tool to infer the ACC nature of these inclusions since analyses can be conducted under native conditions. However, special care has to be taken to minimize irradiation delivered to the cells and check that cells are still covered by a wall. Moreover, we advocate that future studies should prefer the term $CaCO_3$ to calcite or

ACC if they did not characterize the crystallinity of the intracellular granules. Reporting that ACC instead of calcite is the constituent of $CaCO_3$ granules in *Achromatium* cells does not enlighten the mechanisms of formation of these granules. However, it sets new constraints on them such as the requirement of a confinement and the need for a higher saturation level of the solution in which $CaCO_3$ forms. It also modifies the quantitative impact of these biominerals on the physiology of the cells. Last, Jin et al. (2018) highlighted that ACC is widespread in biomineralizing eukaryotes. Here we show that this is also the case in prokaryotes since the presently three known cases of intracellular biomineralization in bacteria, i.e. diverse cyanobacteria, some magnetotactic Alphaproteobacteria and *Achromatium*, all form ACC.

References

Addadi, L., Raz, S., & Weiner, S. (2003). Taking Advantage of Disorder : Amorphous Calcium Carbonate and Its Roles in Biomineralization. *Advanced Materials*, *15*(12), 959-970. https://doi.org/10.1002/adma.200300381

Babenzien, H.-D. (1991). Achromatium oxaliferum and its ecological niche. *Zentralblatt Für Mikrobiologie*, *146*(1), 41-49. https://doi.org/10.1016/S0232-4393(11)80258-1

Babenzien, H.-D., Glöckner, F. O., & Head, I. M. (2015). *Achromatium*. In W. B. Whitman, F. Rainey, P. Kämpfer, M. Trujillo, J. Chun, P. DeVos, B. Hedlund, & S. Dedysh (Éds.), *Bergey's Manual of Systematics of Archaea and Bacteria* (p. 1-8). John Wiley & Sons, Ltd. https://doi.org/10.1002/9781118960608.gbm01222

Behrens, G., Kuhn, L., Ubic, R., & Heuer, A. (1995). Raman-Spectra of Vateritic Calcium-Carbonate. *Spectroscopy Letters*, *28*(6), 983-995. https://doi.org/10.1080/00387019508009934

763 Bentov, S., Brownlee, C., & Erez, J. (2009). The role of seawater endocytosis in the biomineralization
764 process in calcareous foraminifera. *Proceedings of the National Academy of Sciences*,
765 *106*(51), 21500-21504. https://doi.org/10.1073/pnas.0906636106
766 Benzerara, K., Skouri-Panet, F., Li, J., Ferard, C., Gugger, M., Laurent, T., Couradeau, E., Ragon, M.,
767 Cosmidis, J., Menguy, N., Margaret-Oliver, I., Tavera, R., Lopez-Garcia, P., & Moreira, D.
768 (2014). Intracellular Ca-carbonate biomineralization is widespread in cyanobacteria.
769 *Proceedings of the National Academy of Sciences*, *111*(30), 10933-10938.
770 https://doi.org/10.1073/pnas.1403510111
771 Bersa, E. (1926). Über das Vorkommen von kohlensaurem Kalk in einer Gruppe von
772 Schwefelbakterien. *Berichte Der Deutschen Botanischen Gesellschaft*, *44*(7), 474-478.
773 https://doi.org/10.1111/j.1438-8677.1926.tb00996.x
774 Blondeau, M., Sachse, M., Boulogne, C., Gillet, C., Guigner, J.-M., Skouri-Panet, F., Poinsot, M.,
775 Ferard, C., Miot, J., & Benzerara, K. (2018). Amorphous Calcium Carbonate Granules Form
776 Within an Intracellular Compartment in Calcifying Cyanobacteria. *Frontiers in Microbiology*,
777 *9*, 1768. https://doi.org/10.3389/fmicb.2018.01768
778 Bolze, J., Peng, B., Dingenouts, N., Panine, P., Narayanan, T., & Ballauff, M. (2002). Formation and
779 growth of amorphous colloidal CaCO3 precursor particles as detected by time-resolved SAXS.
780 *Langmuir*, *18*(22), 8364–8369.
781 Brečević, L., & Nielsen, A. E. (1989). Solubility of amorphous calcium carbonate. *Journal of Crystal*
782 *Growth*, *98*(3), 504-510. https://doi.org/10.1016/0022-0248(89)90168-1
783 Cam, N., Benzerara, K., Georgelin, T., Jaber, M., Lambert, J.-F., Poinsot, M., Skouri-Panet, F., &
784 Cordier, L. (2016). Selective uptake of alkaline earth metals by cyanobacteria forming
785 intracellular carbonates. *Environmental Science & Technology*, *50*(21), 11654-11662.
786 https://doi.org/10.1021/acs.est.6b02872
787 Carino, A., Testino, A., Andalibi, M. R., Pilger, F., Bowen, P., & Ludwig, C. (2017). Thermodynamic-
788 Kinetic Precipitation Modeling. A Case Study : The Amorphous Calcium Carbonate (ACC)

Precipitation Pathway Unravelled. *Crystal Growth & Design*, *17*(4), 2006-2015. https://doi.org/10.1021/acs.cgd.7b00006

Cavanaugh, J., Whittaker, M. L., & Joester, D. (2019). Crystallization kinetics of amorphous calcium carbonate in confinement. *Chemical Science*, *10*(19), 5039-5043. https://doi.org/10.1039/C8SC05634J

Couradeau, E., Benzerara, K., Gerard, E., Moreira, D., Bernard, S., Brown, G. E., & Lopez-Garcia, P. (2012). An Early-Branching Microbialite Cyanobacterium Forms Intracellular Carbonates. *Science*, *336*(6080), 459-462. https://doi.org/10.1126/science.1216171

DeCarlo, T. M. (2018). Characterizing coral skeleton mineralogy with Raman spectroscopy. *Nature Communications*, *9*(1), 5325. https://doi.org/10.1038/s41467-018-07601-3

Fau, A., Beyssac, O., Gauthier, M., Meslin, P. Y., Cousin, A., Benzerara, K., Bernard, S., Boulliard, J. C., Gasnault, O., Forni, O., Wiens, R. C., Morand, M., Rosier, P., Garino, Y., Pont, S., & Maurice, S. (2019). Pulsed laser-induced heating of mineral phases : Implications for laser-induced breakdown spectroscopy combined with Raman spectroscopy. *Spectrochimica Acta Part B: Atomic Spectroscopy*, *160*, 105687. https://doi.org/10.1016/j.sab.2019.105687

Fernandez-Martinez, A., Kalkan, B., Clark, S. M., & Waychunas, G. A. (2013). Pressure-Induced Polyamorphism and Formation of 'Aragonitic' Amorphous Calcium Carbonate. *Angewandte Chemie International Edition*, *52*(32), 8354-8357. https://doi.org/10.1002/anie.201302974

Glöckner, F. O., Babenzien, H.-D., Wulf, J., & Amann, R. (1999). Phylogeny and Diversity of Achromatium oxaliferum. *Systematic and Applied Microbiology*, *22*(1), 28-38. https://doi.org/10.1016/S0723-2020(99)80025-3

Gower, L. B. (2008). Biomimetic Model Systems for Investigating the Amorphous Precursor Pathway and Its Role in Biomineralization. *Chemical Reviews*, *108*(11), 4551-4627. https://doi.org/10.1021/cr800443h

Gray, N. D., Howarth, R., Pickup, R. W., Jones, J. G., & Head, I. M. (1999). Substrate Uptake by Uncultured Bacteria from the Genus Achromatium Determined by Microautoradiography.

Applied and Environmental Microbiology, *65*(11), 5100-5106. https://doi.org/10.1128/AEM.65.11.5100-5106.1999

Gray, N., & Head, I. (2014). The Family Achromatiaceae. In E. Rosenberg, E. F. DeLong, S. Lory, E. Stackebrandt, & F. Thompson (Éds.), *The Prokaryotes* (p. 1-14). Springer Berlin Heidelberg. https://doi.org/10.1007/978-3-642-38922-1_406

Gray, Neil D. (2006). The Unique Role of Intracellular Calcification in the Genus Achromatium. In J. M. Shively (Éd.), *Inclusions in Prokaryotes* (p. 299-309). Springer. https://doi.org/10.1007/3-540-33774-1_11

Head, I. M., Gray, N. D., Pickup, R. W., & Jones, J. G. (1995). The biogeochemical role of Achromatium oxaliferum. In *Organic Geochemistry : Developments and Applications to Energy, Climate, Environment and Human History* (J. O. Grimalt and C. Dorronsoro, p. 895-898). AlGOA, Donostia-San Sebastian.

Head, Ian M., Gray, N. D., Howarth, R., Pickup, R. W., Clarke, K. J., & Jones, J. G. (2000). Achromatium oxaliferum understanding the unmistakable. In B. Schink (Éd.), *Advances in Microbial Ecology* (Vol. 16, p. 1-40). Springer US. https://doi.org/10.1007/978-1-4615-4187-5_1

Ionescu, D., Bizic-Ionescu, M., De Maio, N., Cypionka, H., & Grossart, H.-P. (2017). Community-like genome in single cells of the sulfur bacterium Achromatium oxaliferum. *Nature Communications*, *8*(1), 455. https://doi.org/10.1038/s41467-017-00342-9

Ionescu, D., Zoccarato, L., Zaduryan, A., Schorn, S., Bižić, M., Pinnow, S., Cypionka, H., & Grossart, H.-P. (2020). Heterozygous, polyploid, giant bacterium, Achromatium, possesses an identical functional inventory worldwide across drastically different ecosystems. *BioRxiv*, 2020.06.06.138032. https://doi.org/10.1101/2020.06.06.138032

Jin, W., Jiang, S., Pan, H., & Tang, R. (2018). Amorphous Phase Mediated Crystallization : Fundamentals of Biomineralization. *Crystals*, *8*(1), 48. https://doi.org/10.3390/cryst8010048

839 Katoh, K., & Standley, D. M. (2013). MAFFT Multiple Sequence Alignment Software Version 7 :
840 Improvements in Performance and Usability. *Molecular Biology and Evolution*, *30*(4),
841 772-780. https://doi.org/10.1093/molbev/mst010
842 Lane, D. J. (1991). 16S/23S rRNA sequencing. In *Nucleic acid techniques in bacterial systematics* (E.
843 Stackebrandt and M. Goodfellow, p. 115-175). John Wiley and Sons.
844 Lassin, A., André, L., Devau, N., Lach, A., Beuvier, T., Gibaud, A., Gaboreau, S., & Azaroual, M. (2018).
845 Dynamics of calcium carbonate formation : Geochemical modeling of a two-step mechanism.
846 *Geochimica et Cosmochimica Acta*, *240*, 236-254. https://doi.org/10.1016/j.gca.2018.08.033
847 Li, J., Margaret Oliver, I., Cam, N., Boudier, T., Blondeau, M., Leroy, E., Cosmidis, J., Skouri-Panet, F.,
848 Guigner, J.-M., Férard, C., Poinsot, M., Moreira, D., Lopez-Garcia, P., Cassier-Chauvat, C.,
849 Chauvat, F., & Benzerara, K. (2016). Biomineralization Patterns of Intracellular
850 Carbonatogenesis in Cyanobacteria : Molecular Hypotheses. *Minerals*, *6*(1), 10.
851 https://doi.org/10.3390/min6010010
852 Liu, Z., Zhang, Z., Wang, Z., Jin, B., Li, D., Tao, J., Tang, R., & De Yoreo, J. J. (2020). Shape-preserving
853 amorphous-to-crystalline transformation of $CaCO_3$ revealed by in situ TEM. *Proceedings of*
854 *the National Academy of Sciences*, *117*(7), 3397-3404.
855 https://doi.org/10.1073/pnas.1914813117
856 Mansor, M., Hamilton, T. L., Fantle, M. S., & Macalady, J. L. (2015). Metabolic diversity and ecological
857 niches of Achromatium populations revealed with single-cell genomic sequencing. *Frontiers*
858 *in Microbiology*, *6*. https://doi.org/10.3389/fmicb.2015.00822
859 Markwardt, C. B. (2009). Non-linear Least Squares Fitting in IDL with MPFIT. *arXiv:0902.2850 [astro-*
860 *ph]*. http://arxiv.org/abs/0902.2850
861 Martignier, A., Pacton, M., Filella, M., Jaquet, J.-M., Barja, F., Pollok, K., Langenhorst, F., Lavigne, S.,
862 Guagliardo, P., Kilburn, M. R., Thomas, C., Martini, R., & Ariztegui, D. (2017). Intracellular
863 amorphous carbonates uncover a new biomineralization process in eukaryotes. *Geobiology*,
864 *15*(2), 240-253. https://doi.org/10.1111/gbi.12213

865 Monteil, C. L., Benzerara, K., Menguy, N., Bidaud, C. C., Michot-Achdjian, E., Bolzoni, R., Mathon, F.
866 P., Coutaud, M., Alonso, B., Garau, C., Jézéquel, D., Viollier, E., Ginet, N., Floriani, M., Swaraj,
867 S., Sachse, M., Busigny, V., Duprat, E., Guyot, F., & Lefevre, C. T. (2020). Intracellular
868 amorphous Ca-carbonate and magnetite biomineralization by a magnetotactic bacterium
869 affiliated to the Alphaproteobacteria. *The ISME Journal*, 1-18.
870 https://doi.org/10.1038/s41396-020-00747-3
871 Moré, J. J. (1978). The Levenberg-Marquardt algorithm : Implementation and theory. In G. A. Watson
872 (Éd.), *Numerical Analysis* (p. 105-116). Springer. https://doi.org/10.1007/BFb0067700
873 Nims, C., Cron, B., Wetherington, M., Macalady, J., & Cosmidis, J. (2019). Low frequency Raman
874 Spectroscopy for micron-scale and in vivo characterization of elemental sulfur in microbial
875 samples. *Scientific Reports*, *9*(1), 7971. https://doi.org/10.1038/s41598-019-44353-6
876 Okada, M., Smith, N. I., Palonpon, A. F., Endo, H., Kawata, S., Sodeoka, M., & Fujita, K. (2012). Label-
877 free Raman observation of cytochrome c dynamics during apoptosis. *Proceedings of the*
878 *National Academy of Sciences*, *109*(1), 28-32. https://doi.org/10.1073/pnas.1107524108
879 Pätzold, R., Keuntje, M., Theophile, K., Müller, J., Mielcarek, E., Ngezahayo, A., & Anders-von Ahlften,
880 A. (2008). In situ mapping of nitrifiers and anammox bacteria in microbial aggregates by
881 means of confocal resonance Raman microscopy. *Journal of Microbiological Methods*, *72*(3),
882 241-248. https://doi.org/10.1016/j.mimet.2007.12.003
883 Perrin, J., Vielzeuf, D., Laporte, D., Ricolleau, A., Rossman, G. R., & Floquet, N. (2016). Raman
884 characterization of synthetic magnesian calcites. *American Mineralogist*, *101*(11), 2525-2538.
885 https://doi.org/10.2138/am-2016-5714
886 Politi, Y., Levi-Kalisman, Y., Raz, S., Wilt, F., Addadi, L., Weiner, S., & Sagi, I. (2006). Structural
887 Characterization of the Transient Amorphous Calcium Carbonate Precursor Phase in Sea
888 Urchin Embryos. *Advanced Functional Materials*, *16*(10), 1289-1298.
889 https://doi.org/10.1002/adfm.200600134

890 Purgstaller, B., Goetschl, K. E., Mavromatis, V., & Dietzel, M. (2019). Solubility investigations in the
891 amorphous calcium magnesium carbonate system. *CrystEngComm*, *21*(1), 155-164.
892 https://doi.org/10.1039/C8CE01596A
893 Salman, V., Yang, T., Berben, T., Klein, F., Angert, E., & Teske, A. (2015). Calcite-accumulating large
894 sulfur bacteria of the genus Achromatium in Sippewissett Salt Marsh. *The ISME Journal*,
895 *9*(11), 2503-2514. https://doi.org/10.1038/ismej.2015.62
896 Schewiakoff, W. (1893). *Uber einen neuen bakteriennähnlichen Organismus des Süßwassers*
897 [Habilitationsschrift]. Heidelberg.
898 Schmidt, I., & Wagermaier, W. (2017). Tailoring Calcium Carbonate to Serve as Optical Functional
899 Material : Examples from Biology and Materials Science. *Advanced Materials Interfaces*, *4*(1),
900 1600250. https://doi.org/10.1002/admi.201600250
901 Schorn, S., & Cypionka, H. (2018). A Crispy Diet : Grazers of Achromatium oxaliferum in Lake Stechlin
902 Sediments. *Microbial Ecology*, *76*(3), 584-587. https://doi.org/10.1007/s00248-018-1158-4
903 Schorn, S., Salman-Carvalho, V., Littmann, S., Ionescu, D., Grossart, H.-P., & Cypionka, H. (2020). Cell
904 Architecture of the Giant Sulfur Bacterium Achromatium oxaliferum : Extra-cytoplasmic
905 Localization of Calcium Carbonate Bodies. *FEMS Microbiology Ecology*, *96*(2), fiz200.
906 https://doi.org/10.1093/femsec/fiz200
907 Stamatakis, A. (2014). RAxML version 8 : A tool for phylogenetic analysis and post-analysis of large
908 phylogenies. *Bioinformatics*, *30*(9), 1312-1313.
909 https://doi.org/10.1093/bioinformatics/btu033
910 Talavera, G., & Castresana, J. (2007). Improvement of Phylogenies after Removing Divergent and
911 Ambiguously Aligned Blocks from Protein Sequence Alignments. *Systematic Biology*, *56*(4),
912 564-577. https://doi.org/10.1080/10635150701472164
913 Váczi, T. (2014). A new, simple approximation for the deconvolution of instrumental broadening in
914 spectroscopic band profiles. *Applied Spectroscopy*, *68*(11), 1274-1278.
915 https://doi.org/10.1366/13-07275

916 Virieux, J. (1913). Recherches sur l'Achromatium oxaliferum. *Annales des Sciences Naturelles*, *18*(1-2),
917 265-288.
918 Wang, D., Hamm, L. M., Bodnar, R. J., & Dove, P. M. (2012). Raman spectroscopic characterization of
919 the magnesium content in amorphous calcium carbonates : Raman spectroscopic
920 characterization. *Journal of Raman Spectroscopy*, *43*(4), 543-548.
921 https://doi.org/10.1002/jrs.3057
922 Wang, H.-W., Daemen, L. L., Cheshire, M. C., Kidder, M. K., Stack, A. G., Allard, L. F., Neuefeind, J.,
923 Olds, D., Liu, J., & Page, K. (2017). Synthesis and structure of synthetically pure and
924 deuterated amorphous (basic) calcium carbonates. *Chemical Communications*, *53*(20),
925 2942-2945. https://doi.org/10.1039/C6CC08848A
926 Wehrmeister, U., Jacob, D. E., Soldati, A. L., Loges, N., Häger, T., & Hofmeister, W. (2011).
927 Amorphous, nanocrystalline and crystalline calcium carbonates in biological materials.
928 *Journal of Raman Spectroscopy*, *42*(5), 926-935. https://doi.org/10.1002/jrs.2835
929 Weiner, S. (2005). STRUCTURAL BIOLOGY : Choosing the Crystallization Path Less Traveled. *Science*,
930 *309*(5737), 1027-1028. https://doi.org/10.1126/science.1114920
931 West, G. S., & Griffiths, B. M. (1913). The Lime-Sulphur Bacteria of the Genus Hillhousia. *Annals of*
932 *Botany*, *os-27*(1), 83-91. https://doi.org/10.1093/oxfordjournals.aob.a089453
933 Xiao, M., Salam, N., Liu, L., Jiao, J.-Y., Zheng, M.-L., Wang, J., Li, S., Chen, C., Li, W.-J., & Qu, P.-H.
934 (2018). Fastidiosibacter lacustris gen. Nov., sp. Nov., isolated from a lake water sample, and
935 proposal of Fastidiosibacteraceae fam. Nov. Within the order Thiotrichales. *International*
936 *Journal of Systematic and Evolutionary Microbiology*, *68*(1), 347-352.
937 https://doi.org/10.1099/ijsem.0.002510
938 Yang, T., Teske, A., Ambrose, W., Salman-Carvalho, V., Bagnell, R., & Nielsen, L. P. (2019). Intracellular
939 calcite and sulfur dynamics of Achromatium cells observed in a lab-based enrichment and
940 aerobic incubation experiment. *Antonie van Leeuwenhoek*, *112*(2), 263-274.
941 https://doi.org/10.1007/s10482-018-1153-2

Zeng, Y., Cao, J., Wang, Z., Guo, J., Zhou, Q., & Lu, J. (2018). Insights into the Confined Crystallization in Microfluidics of Amorphous Calcium Carbonate. *Crystal Growth & Design*, *18*(11), 6538-6546. https://doi.org/10.1021/acs.cgd.8b00675

Zou, Z., Yang, X., Alberic, M., Heil, T., Wang, Q., Pokroy, B., Politi, Y., & Bertinetti, L. (2020). Additives Control the Stability of Amorphous Calcium Carbonate via Two Different Mechanisms : Surface Adsorption versus Bulk Incorporation. *Advanced Functional Materials*, *30*(23), 2000003. https://doi.org/10.1002/adfm.202000003

Supplementary information of "The gamaproteobacterium Achromatium forms intracellular amorphous calcium carbonate and not (crystalline) calcite"

Supplementary information file contains 5 figures and 1 table

References	Techniques used	Affiliation to ACC or calcite?
West and Griffiths (1913); Bersa (1926)	Chemical treatments and optical microscopy	ACC
Head et al. (2000)	x-ray diffraction	Calcite
Gray (2006)	Same x-ray diffraction data as Head et al. (2000)	Calcite that "may not be purely crystalline"
Salman et al. (2015)	Raman spectroscopy	calcite
Yang et al. (2019)	Observations of laminations in $CaCO_3$ granules by focused Ion beam	Calcite but also mention "colloidal calcite"
Schorn et al. (2020)	Chemical treatments and optical microscopy	Mention mostly calcium carbonate, sometimes calcite but notice that upon some treatments "cubic calcium carbonate crystals" formed outside of the cells

Table S1: Summary of how intracellular $CaCO_3$ granules in *Achromatium* were named and identified by some studies.

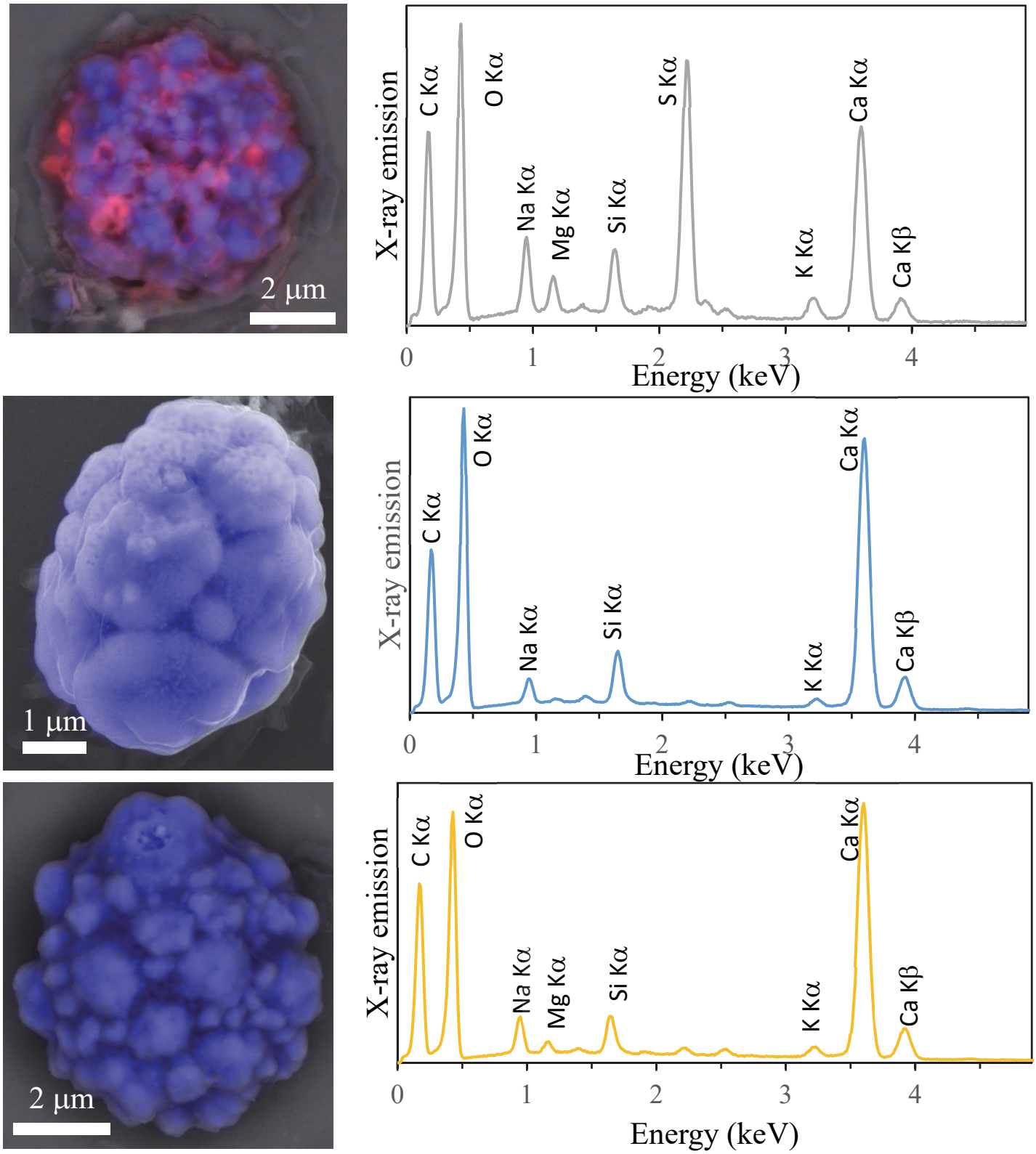

Figure S1: SEM-EDXS analyses of the *Achromatium* cells analyzed by Raman. On the left, overlays of the image obtained in the backscattered electron mode (ASB detector) and the Ca (and S in the top and bottom lines) map. On the right, EDXS spectra of the whole cells. Top: Cell showing a Raman spectrum characteristic of S^0 (see Figure 3). Following lines: cells showing a Raman spectrum characteristic of ACC (e.g., see Figure 4). Only very little S is detected in the two bottom lines in comparison with the top line.

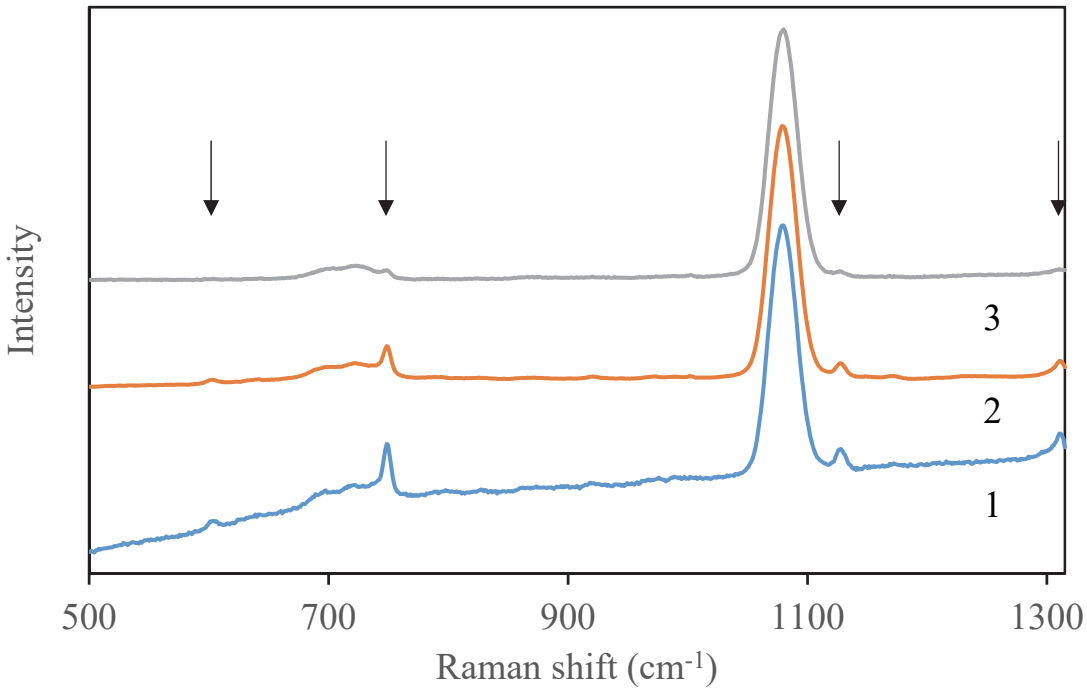

Figure S2: Raman spectra measured consecutively (from the bottom to the top) on the same spot. The three spectra were normalized in intensity relatively to the height of the ν1 band of ACC at ~1079 cm^{-1}. (1) with 1% of laser power and 50 accumulations; (2) 10% of laser power and 20 accumulations; (3) 1% of laser power and 50 accumulations. Arrows show bands related to cytochromes at 604.4, 749.4, 1128 and 1311 cm^{-1}.

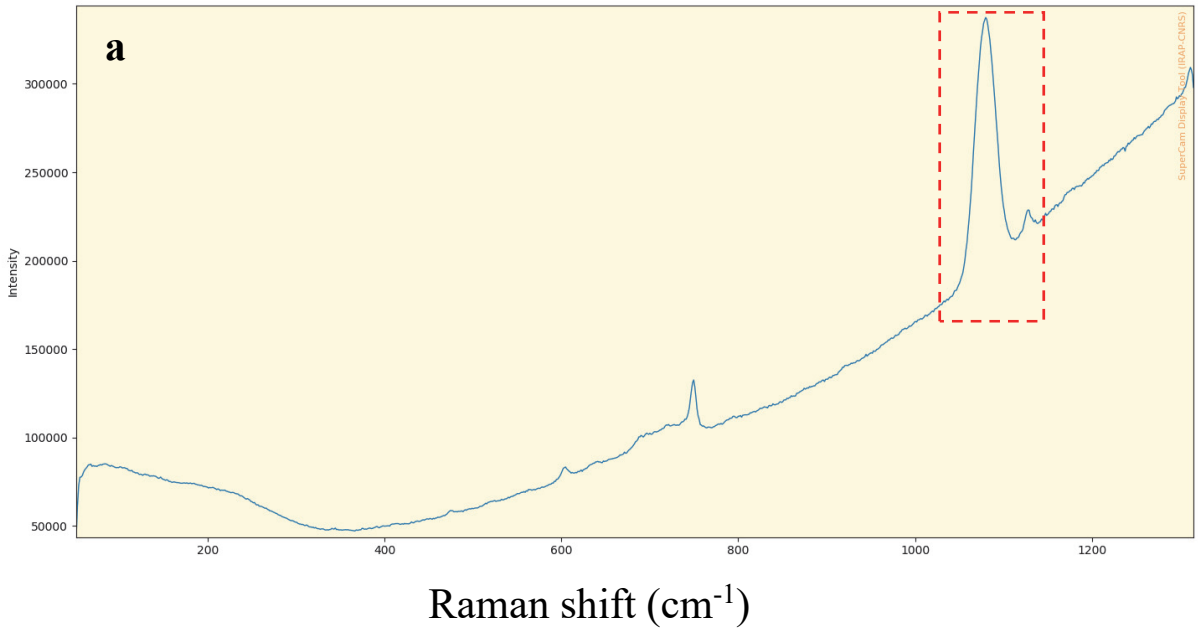
a
Intensity
Raman shift (cm-1)

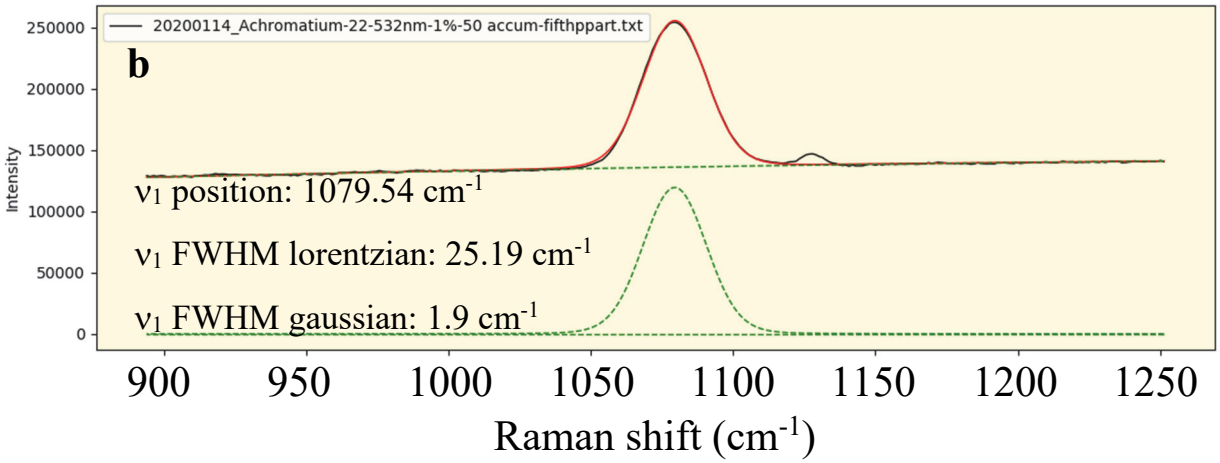
20200114_Achromatium-22-532nm-1%-50 accum-fifthppart.txt
b
ν1 position: 1079.54 cm-1
ν1 FWHM lorentzian: 25.19 cm-1
ν1 FWHM gaussian: 1.9 cm-1
Intensity
Raman shift (cm-1)

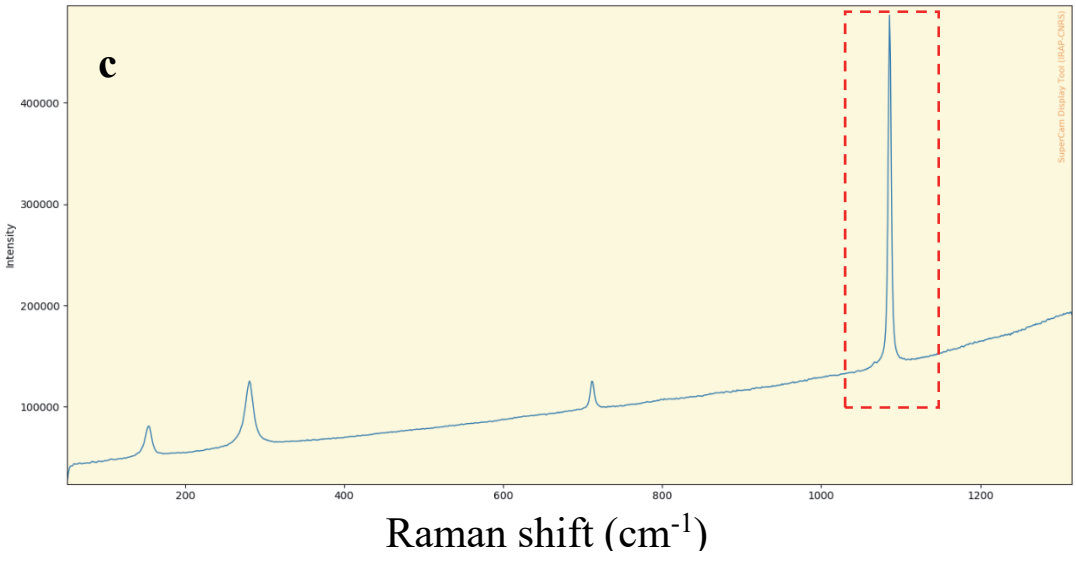
c
Intensity
Raman shift (cm-1)

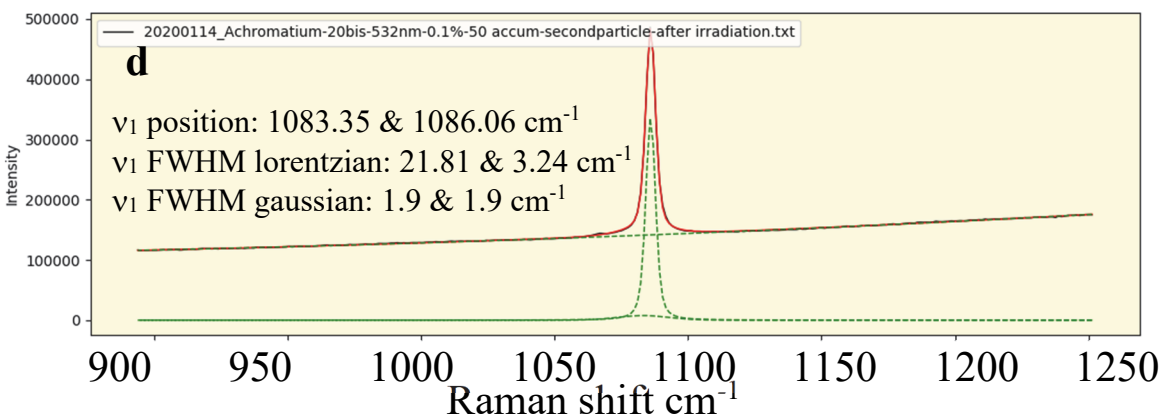
20200114_Achromatium-20bis-532nm-0.1%-50 accum-secondparticle-after irradiation.txt
d
ν1 position: 1083.35 & 1086.06 cm-1
ν1 FWHM lorentzian: 21.81 & 3.24 cm-1
ν1 FWHM gaussian: 1.9 & 1.9 cm-1
Intensity
Raman shift cm-1

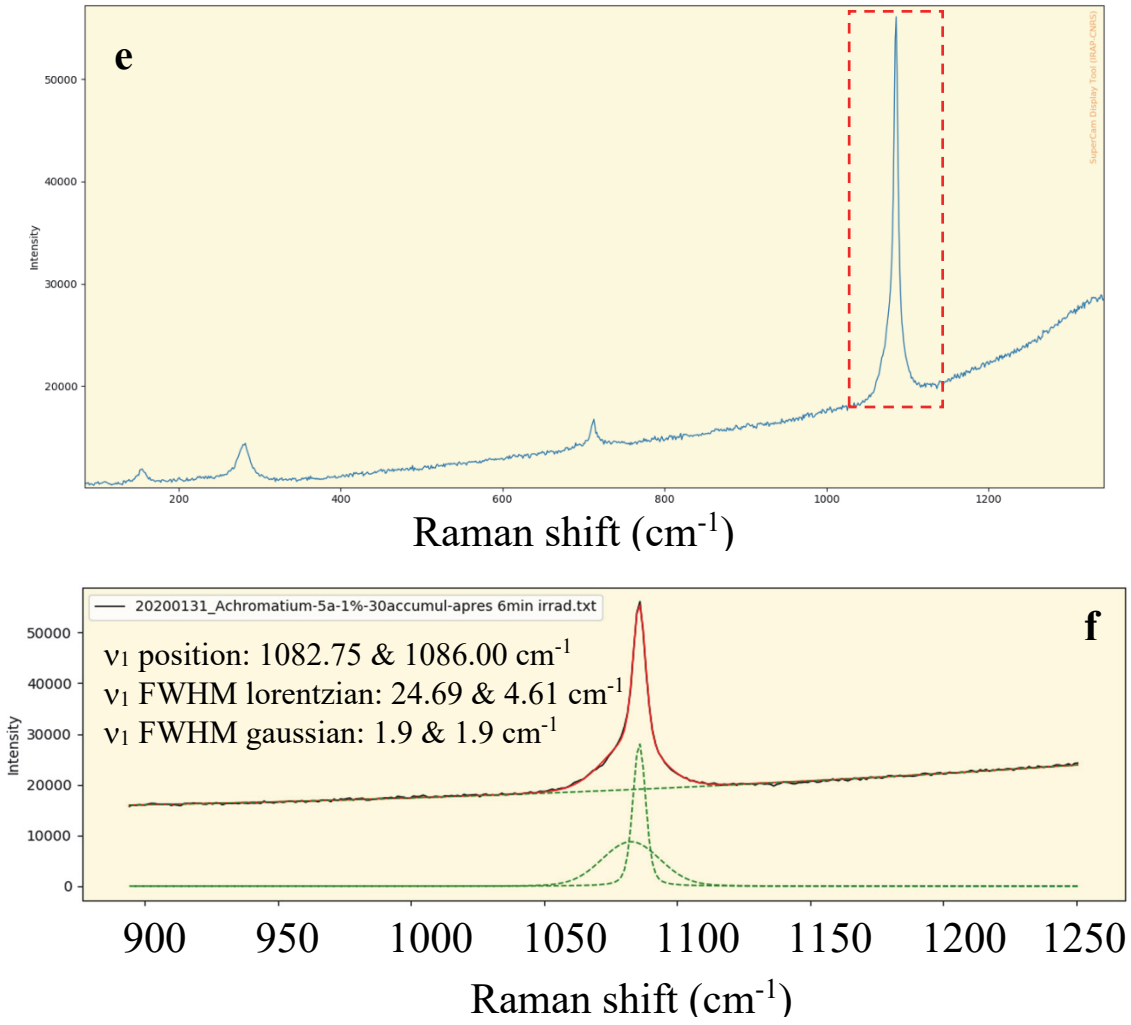

Figure S3: Fit of the Raman ν_1 bands. (a) Raman spectrum of an ACC granule. (b) Fit of the ν_1 band with one Voigt function. The solid black line shows the data. The solid red line shows the Voigt fit. The dashed green line shows the linear background correction. The data and the fit superimpose very well except at ~1127.9 cm^{-1} where the cytochrome band was not fitted here. The values of the ν_1 position and Lorentzian and Gaussian FWHMs are provided. (c) and (d) same for a granule transformed into calcite by irradiation. (e) and (f) same but in the latter case, the resulting ν_1 band shows a clear asymmetry which could be fitted using two significant Voigt functions.

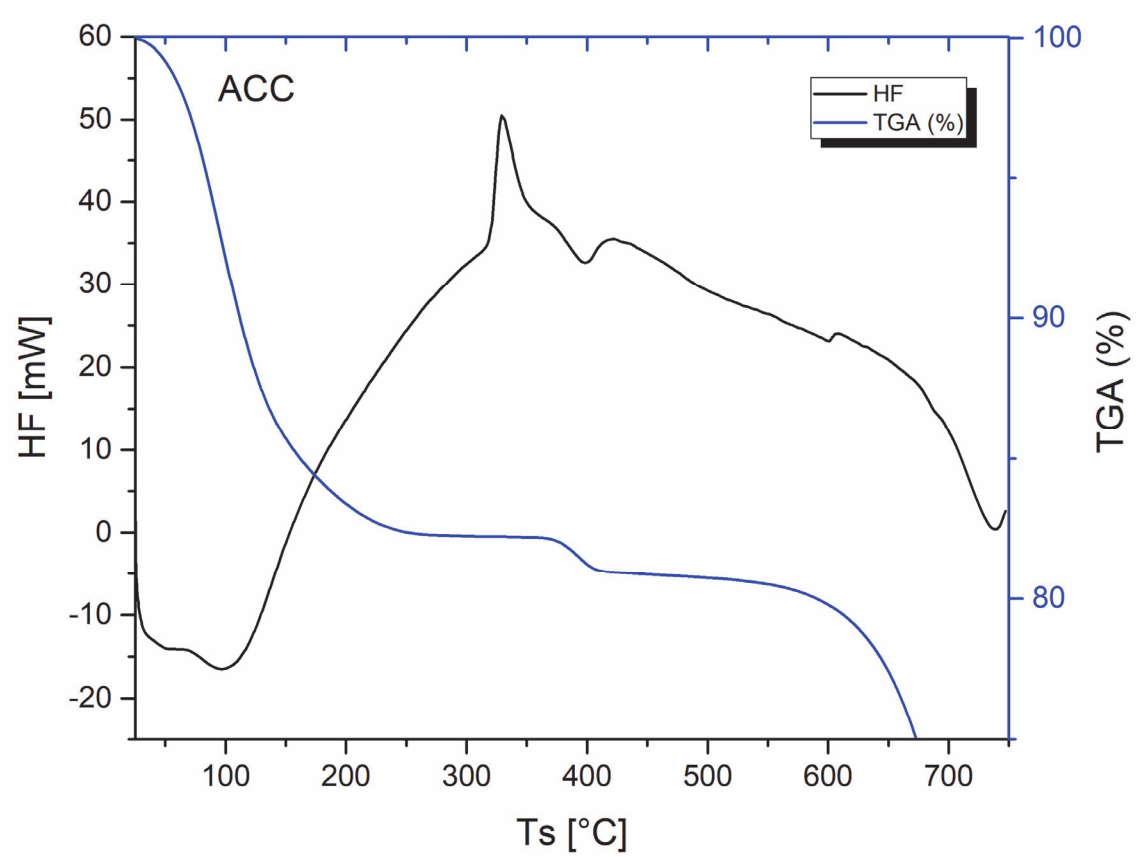

Figure S4: Thermogravimetric analysis of a synthetic ACC compound showing an exothermic peak at 330 °C, which indicates crystallization into calcite.